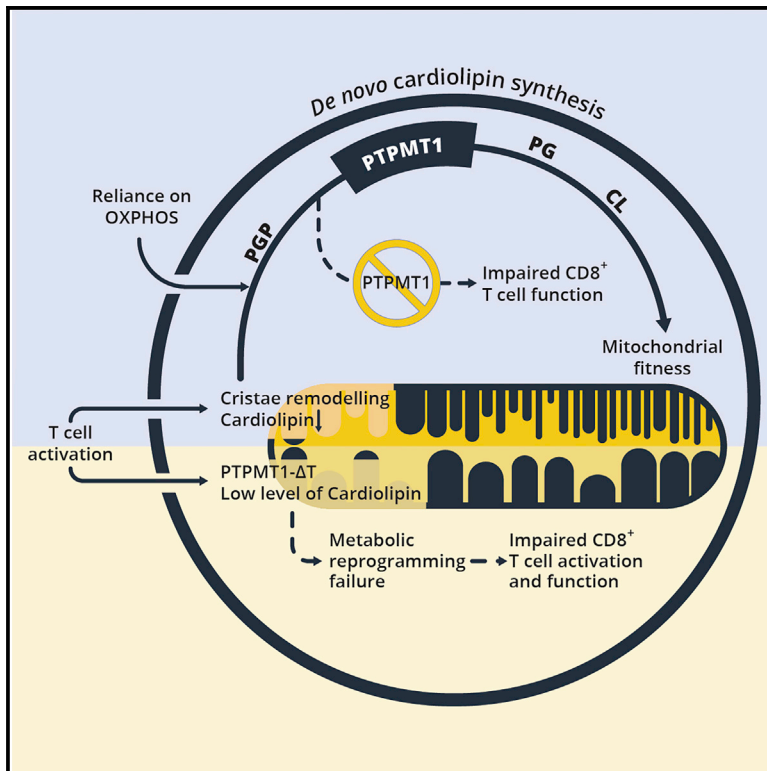# Dynamic Cardiolipin Synthesis Is Required for CD8+ T Cell Immunity

Graphical Abstract

Authors

Mauro Corrado, Joy Edwards-Hicks, Matteo Villa, ..., David O'Sullivan, Edward J. Pearce, Erika L. Pearce

Correspondence

pearce@ie-freiburg.mpg.de

In Brief

Corrado et al. show that the mitochondrial membrane-specific lipid cardiolipin is required for the metabolic plasticity that is essential for effective CD8+ T cell function. Cardiolipin-deficient CD8+ T cells fail to respond to pathogens and are not able to adapt to nutrient stress.

Highlights

- Cardiolipin is essential for *in vivo* and *in vitro* CD8+ T cell responses

- Active cardiolipin synthesis and remodeling occurs during T cell differentiation

- Cardiolipin synthesis supports CD8+ T_M cell development, metabolism, and function

- T cell defects are evident in TAZ KO mice and in Barth syndrome patients

Article

Dynamic Cardiolipin Synthesis Is Required for CD8+ T Cell Immunity

Mauro Corrado,[1] Joy Edwards-Hicks,[1] Matteo Villa,[1] Lea J. Flachsmann,[1] David E. Sanin,[1] Maaike Jacobs,[1] Francesc Baixauli,[1] Michal Stanczak,[1] Eve Anderson,[2] Mai Azuma,[1] Andrea Quintana,[1] Jonathan D. Curtis,[1] Thomas Clapes,[1] Katarzyna M. Grzes,[1] Agnieszka M. Kabat,[1] Ryan Kyle,[1] Annette E. Patterson,[1] Ramon Klein Geltink,[1] Borko Amulic,[3] Colin G. Steward,[3] Douglas Strathdee,[2] Eirini Trompouki,[1] David O'Sullivan,[1] Edward J. Pearce,[1,4] and Erika L. Pearce[1,5,*]

[1]Max-Planck Institute of Immunobiology and Epigenetics, 79108 Freiburg, Germany
[2]Cancer Research UK Beatson Institute, Glasgow G61 1 BD, UK
[3]School of Cellular and Molecular Medicine, University of Bristol, Bristol BS8 1TH, UK
[4]Faculty of Biology, University of Freiburg, 79098 Freiburg im Breisgau, Germany
[5]Lead Contact
*Correspondence: pearce@ie-freiburg.mpg.de
https://doi.org/10.1016/j.cmet.2020.11.003

SUMMARY

Mitochondria constantly adapt to the metabolic needs of a cell. This mitochondrial plasticity is critical to T cells, which modulate metabolism depending on antigen-driven signals and environment. We show here that *de novo* synthesis of the mitochondrial membrane-specific lipid cardiolipin maintains CD8+ T cell function. T cells deficient for the cardiolipin-synthesizing enzyme PTPMT1 had reduced cardiolipin and responded poorly to antigen because basal cardiolipin levels were required for activation. However, neither *de novo* cardiolipin synthesis, nor its Tafazzin-dependent remodeling, was needed for T cell activation. In contrast, PTPMT1-dependent cardiolipin synthesis was vital when mitochondrial fitness was required, most notably during memory T cell differentiation or nutrient stress. We also found CD8+ T cell defects in a small cohort of patients with Barth syndrome, where *TAFAZZIN* is mutated, and in a *Tafazzin*-deficient mouse model. Thus, the dynamic regulation of a single mitochondrial lipid is crucial for CD8+ T cell immunity.

INTRODUCTION

Upon activation, CD8+ T cells shift from a quiescent to a highly active metabolic state where both glycolysis and OXPHOS increase (Bailis et al., 2019; Buck et al., 2017; Chang et al., 2013; Geltink et al., 2018; Klein Geltink et al., 2017; Sena et al., 2013). During this phase, mitochondria generate signals, such as reactive oxygen species (ROS) or metabolites, required to drive T cell differentiation (Bailis et al., 2019; Sena et al., 2013). Although effector T (T$_E$) cells increase aerobic glycolysis during *in vitro* culture, they display greater rates of oxidative phosphorylation (OXPHOS) *in vivo* (Ma et al., 2019). When the infection or cancer has been eradicated, the majority of T$_E$ cells die, leaving behind a small number of long-lived memory T (T$_M$) cells that confer long-term immune protection. T$_M$ cells engage catabolic pathways like fatty acid oxidation (FAO) to fuel mitochondrial respiration (Pearce et al., 2009; van der Windt et al., 2012). Overall, cellular metabolic changes supported by mitochondria are integral to a functional T cell response.

Mitochondria continuously undergo fusion and fission (Chan, 2020; Pernas and Scorrano, 2016), and Optic atrophy 1 (OPA1), a protein critical for mitochondrial shape and metabolism (Cipolat et al., 2004; Cogliati et al., 2013; Frezza et al., 2006), is required to generate T$_M$ cells (Buck et al., 2016). Mito-

chondria also differ at the sub-organellar level, where different properties and lipid compositions exist between the inner (IMM) and outer mitochondrial membrane (OMM) (Frey and Mannella, 2000). The IMM is organized in discrete invaginations called cristae, where electron transport chain (ETC) complexes are located (Mannella et al., 2001; Wolf et al., 2019). Cardiolipin (CL) is exclusively synthesized and localized in the IMM and accounts for 15%–20% of the total phospholipid mass (Dudek, 2017). CL is a four-acyl chain lipid with a small negative glycerol polar head responsible for the negative curvature of the cristae. Here, CL binds to ETC complexes, making respiration more efficient and reducing ROS (Paradies et al., 2014), and also modulates substrate carrier activity and protein import (Paradies et al., 2019). When mislocalized to the OMM, CL recruits caspases, promoting apoptosis or triggering an inflammatory response (Gonzalvez et al., 2008; Iyer et al., 2013). In addition to its role in heart and muscle (Dudek et al., 2019), CL synthesis is essential for systemic energy homeostasis to prevent insulin resistance (Sustarsic et al., 2018).

CL composition varies greatly in both acyl chain length and saturation, with the tetra-linoleic form (CL 72:8) being the most abundant species (Minkler and Hoppel, 2010). CL localization at the site of OXPHOS makes it susceptible to oxidation by cytochrome *c* (Kagan et al., 2005). When oxidation occurs,
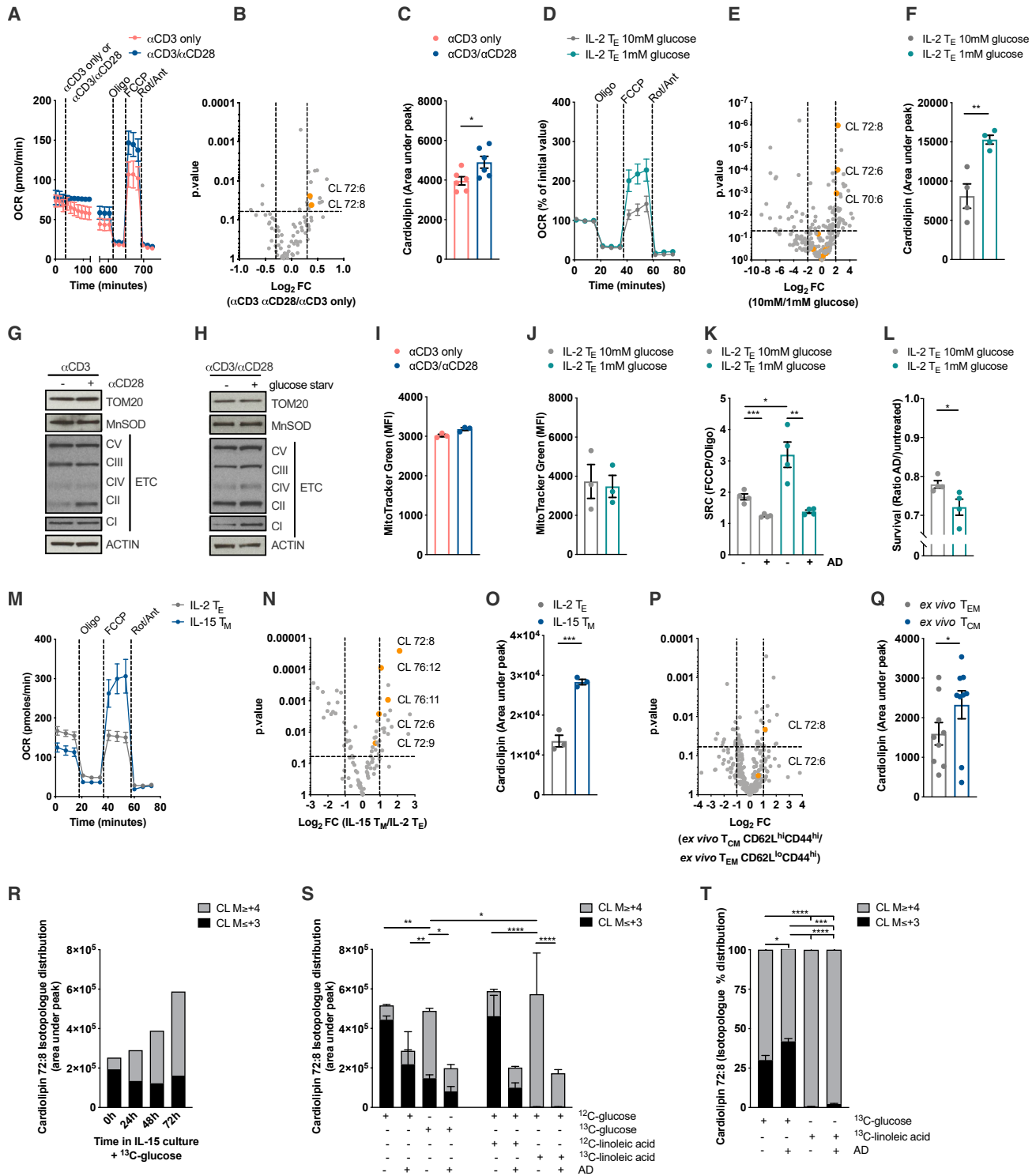
Figure 1. *De Novo* Cardiolipin Synthesis Is a Hallmark of CD8+ T Cells with a High-Reserve Respiratory Capacity

(A) OCR of mouse WT CD8+ T cells activated with αCD3 only or αCD3/αCD28 and differentiated in IL-15 T_M cells for 6 days. OCR analysis at baseline and after exposure to αCD3/αCD28 coated beads, Oligomycin (Oligo), FCCP, and Rotenone/Antimycin (Rot/Ant).

(B) Lipids extracted from cells activated and differentiated as in (A). Data show Log2FC and p value calculated with ANOVA test.

(C) Total CL content in cells treated and analyzed as in (B).

(D) OCR of mouse WT CD8+ T cells activated with αCD3/αCD28 + IL-2 and cultured in complete medium until day 3, then cultured for 24 h in either complete medium (10mM glucose) or glucose restricted medium (1mM glucose) for 24 h. Normalized OCR at baseline and after (Oligo) FCCP and Rot/Ant injections.

(legend continued on next page)

phospholipases remove the altered acyl chain, generating an intermediate monolysocardiolipin (MLCL), which is then "remodeled" into mature CL by the enzyme TAFAZZIN (Hsu et al., 2013; Schlame, 2013). Mutations in *TAFAZZIN* result in reduced CL content in all cells (Schlame et al., 2003) and are responsible for Barth syndrome, an X-linked recessive human disease characterized by dilated cardiomyopathy, muscle weakness, and fatigue (Barth et al., 1983; Bione et al., 1996; Clarke et al., 2013). Neutropenia and susceptibility to infections have been reported in 90% of Barth syndrome patients, but mechanistic analyses into the impaired immunity is lacking (Steward et al., 2019). Clinically relevant total lymphopenia has only been described in one Barth syndrome patient, where it was a prelude to development of non-Epstein Barr virus (EBV)-associated T cell non-Hodgkin lymphoma following cardiac transplantation (Ronghe et al., 2001).

Our previous work has shown how changes in mitochondrial shape, cristae morphology, and function directly impact CD8^{+} T cell activation, differentiation, and functional T_M cell development (Buck et al., 2016; Klein Geltink et al., 2017; van der Windt et al., 2012). The role of CL presence, *de novo* synthesis, or remodeling in the assumption of distinct metabolic programs and mitochondrial function in T cells has not been investigated. Given these collective observations, and the pivotal function of CL in regulating OXPHOS and cristae structure, we set out to investigate the role of CL in the CD8^{+} T cell response.

RESULTS

De Novo Synthesis of Cardiolipin Is a Hallmark of CD8^{+} T Cells with High-Reserve Respiratory Capacity

We investigated how CL was modulated in CD8^{+} T cell culture settings that invoked higher spare respiratory capacity (SRC), a measure of a cell's ability to make extra ATP from OXPHOS upon increased energy demand (Nicholls, 2009). CD28 co-stim-

ulation during activation promotes SRC in T_M cells generated *in vitro* with IL-15 (Figure 1A) and is also required for the generation of functional T_M cells *in vivo* (Klein Geltink et al., 2017). We analyzed lipids from interleukin (IL)-15 T_M cells activated with αCD3 or with αCD3/αCD28 and observed higher CL72:8 and CL72:6 (Figure 1B) as well as total CL content (Figure 1C) in cells activated with CD28 co-stimulation. Nutrient restriction also induces CD28-dependent mitochondrial elongation in CD8^{+} T cells (Klein Geltink et al., 2017) and the assembly of ETC supercomplexes in order to sustain viability and protect from cell death (Gomes et al., 2011). Thus, we generated *in vitro* IL-2 T_E cells and cultured them in 1 mM versus 10 mM glucose for 20 h before analyzing lipid composition. Culturing IL-2 T_E cells in 1 mM glucose for 20 h generated higher SRC (Figure 1D) (Klein Geltink et al., 2017). Lipidomics analysis revealed that various CL species were significantly enriched in 1 mM glucose (Figure 1E), increasing overall CL content (Figure 1F). We obtained similar results culturing IL-2 CD8^{+} T_E cells in a medium containing 10 mM galactose (instead of glucose) to force mitochondrial respiration (Chang et al., 2013) (data not shown). Of note, the metabolic rewiring that led to increased CL content (Figures 1B–1F) occurred without an increase in mitochondrial mass measured by TOM20 and MnSOD, ETC protein levels (Figures 1G, 1H, S1A, and S1B), MitoTracker Green dye accumulation (Figures 1I and 1J), and mtDNA/nuclear DNA (nDNA) ratio (Figures S1C and S1D). *De novo* CL synthesis in the 1 mM condition was needed to generate higher SRC and protect cells from starvation-induced death as these cells lost SRC (Figure 1K) and viability (Figure 1L) when treated with the PTPMT1-specific inhibitor alexidine dihydrochloride (AD).

In vitro generated IL-15 T_M cells are characterized by higher SRC (Figure 1M) as well as by elongated mitochondria together with greater mitochondrial mass (Buck et al., 2016; van der Windt et al., 2012). These cells also displayed a selective enrichment in CL (Figures 1N, 1O, and S1E), accompanied by higher

(E) Lipids extracted from cells activated and differentiated as in (F). Data show Log2FC and p value calculated with ANOVA test.

(F) Total CL content in cells treated and analyzed as in (F).

(G) Immunoblot analysis of cells activated and differentiated as in (A).

(H) Immunoblot analysis of cells treated as in (D).

(I) MitoTracker Green staining in cells activated and differentiated as in (A).

(J) MitoTracker Green staining in cells activated and differentiated as in (D).

(K) SRC of CD8^{+} T cells activated as in (D) and cultured ± AD during 20 h of glucose restriction.

(L) Survival of CD8^{+} T cells activated as in (D) and cultured ± AD during 20 h of glucose restriction.

(M) OCR of mouse WT CD8^{+} T cells activated with αCD3/αCD28 + IL-2 and cultured in complete medium until day 3, then for additional three days in IL-2 (IL-2 T_E) or IL-15 (IL-15 T_M).

(N) Lipids extracted from WT CD8^{+} T cells differentiated as in (M). Data show Log2FC and p value calculated with ANOVA test.

(O) Total CL content from IL-2 T_E and IL-15 T_M CD8^{+} T cells cultured as in (M).

(P) Lipids extracted from T_{EM} (CD44^{hi}CD62L^{lo}) and T_{CM} (CD44^{hi}CD62L^{hi}) cells isolated *ex vivo* from C57BL/6 mice. Data show Log2FC and p value calculated with ANOVA test from 9 animals per group.

(Q) Total CL content from T_{EM} and T_{CM} cells isolated as in (P). Dots represent individual mice.

(R) CD8^{+} T cells were activated with αCD3/αCD28 + IL-2 for 3 days and then differentiated into IL-15 T_M cells in presence of ^{13}C-glucose. At indicated time points lipids were extracted and ^{13}C-glucose derived carbons traced into CL 72:8.

(S) CD8^{+} T cells were activated with αCD3/αCD28 + IL-2 for 3 days and then differentiated into IL-15 T_M cells for 72 h in the presence of ^{13}C-glucose or ^{13}C-linoleic acid ± CL synthesis inhibitor (AD). ^{13}C-glucose and ^{13}C-linoleic acid derived carbons traced into CL 72:8.

(T) CD8^{+} T cells were differentiated as in (S). Also shown is the percentage of isotopologue distribution of ^{13}C-glucose and ^{13}C-linoleic acid-derived carbons traced into CL 72:8.

Data shown as mean ± SEM of ≥3 independent experiments unless indicated. Statistical comparisons for two groups calculated by unpaired two-tailed Student's t test or ANOVA test, where indicated. Comparison among multiple groups (in [R] and [S]) calculated by One-Way ANOVA and correcting for multiple comparison using Tukey test. *p < 0.05; **p < 0.01; ***p < 0.001.
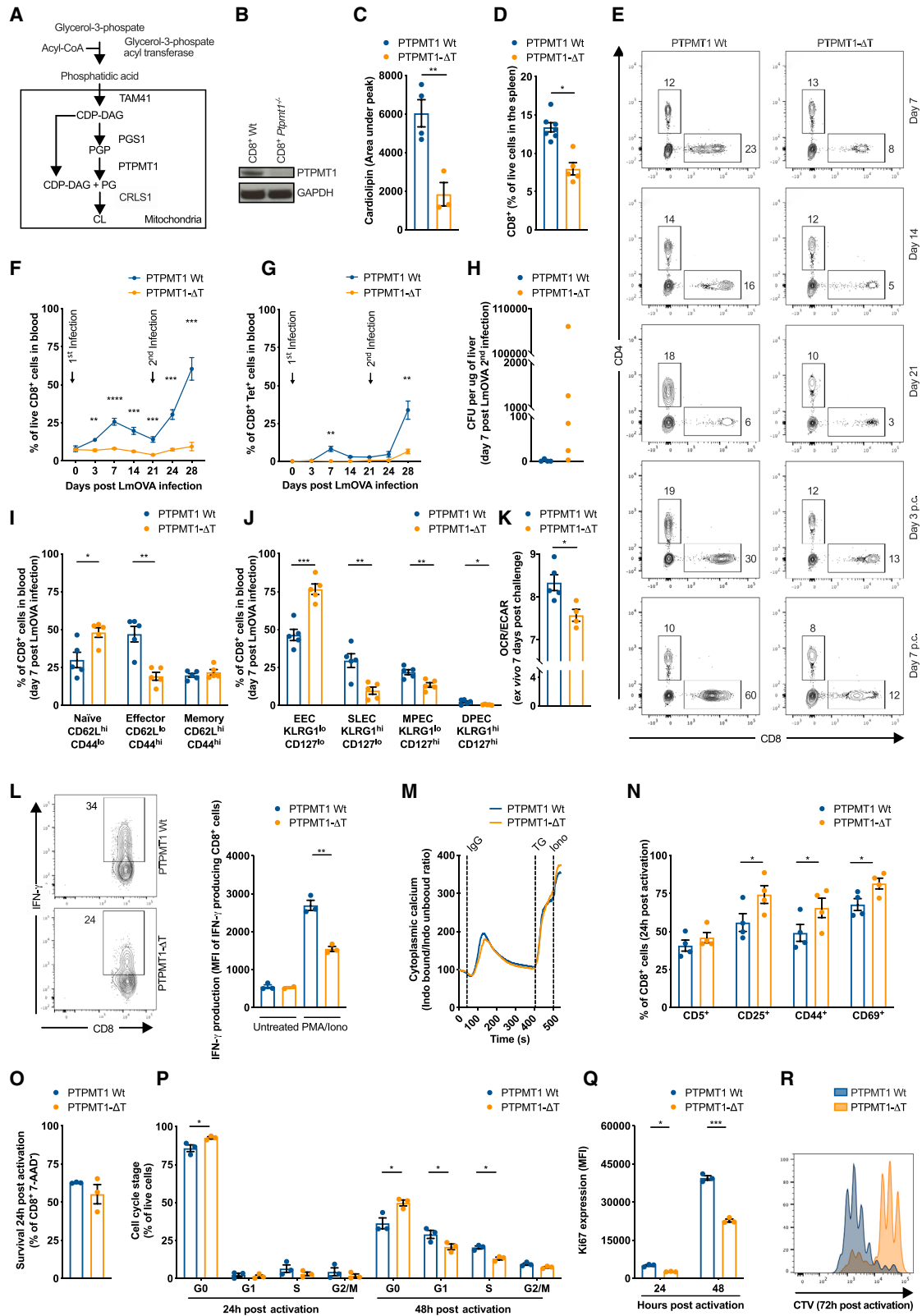
See also Figure S1.

Figure 2. Cardiolipin Is Necessary for *In Vivo* and *In Vitro* CD8$^+$ T Cell Responses

(A) Schematic of the cardiolipin synthesis pathway.

(B) PTPMT1 expression in CD8$^+$ T cells from PTPMT1 WT (*Ptpmt1$^{flox/flox}$*CD4-Cre$^{-/-}$) and PTPMT1-ΔT (*Ptpmt1$^{flox/flox}$*CD4-Cre$^{+/-}$) mice.

expression of PTPMT1 and CRLS1 (Figure S1F), as compared to what was seen in IL-2 T_E cells. Although there was up to a 1.5-/2-fold difference in mitochondrial mass observed between IL-2 T_E and IL-15 T_M cells (considering mtDNA/nDNA ratio or TFAM expression; van der Windt et al., 2012), the CL amount increased almost three times, suggesting a specific enrichment in CL in the mitochondria of IL-15 T_M cells. *In vitro* culture and *in vivo* differentiation of T cells could be different (Ma et al., 2019). Therefore, we sorted CD8$^+$ T effector memory (T_{EM} CD62L^{lo}CD44^{hi}) and CD8$^+$ T central memory (T_{CM} CD62L^{hi}CD44^{hi}) cells from the same animal and analyzed their lipid composition. Lipidomics analysis showed CL 72:8 among the most significantly enriched lipids (Figures 1P and S1G) and almost exclusively responsible for the increase in total CL mass in CD8$^+$ T_{CM} cells (Figure 1Q). Notably, human (h) CD8$^+$CD45RO$^+$ T_{EM} cells also had a higher basal and maximal respiration rate than did hCD8$^+$CD45RA$^+$ naive T (T_N) cells (Figure S1H). They also exhibited, although with higher variability, a trend toward the enrichment of specific CL species (Figure S1I) and higher total CL content (Figure S1J), without major changes in mitochondrial mass (Figure S1K). Taken together these data suggest that T cells, upon stimuli that provoke mitochondrial respiration (e.g., CD28 co-stimulation, glucose restriction, galactose culture, or IL-15 supported T_M cell development), rewire metabolism to increase mitochondrial efficiency through *de novo* cardiolipin synthesis before, or independently from, mitochondrial biogenesis.

Substrate Utilization Reveals Active *De Novo* Cardiolipin Synthesis and Remodeling during T_M Cell Differentiation

To gain insight into the metabolic rewiring responsible for the increase in CL content in IL-15 T_M cells, we performed ^{13}C-glucose and ^{13}C-linoleic acid tracing to measure incorporation of labeled carbons into CL. The first was used to measure whether the classic energetic substrate of IL-15 T_M cells was used for *de novo* CL synthesis (O'Sullivan et al., 2014), the latter to investigate CL remodeling by the acyltransferase TAFAZZIN, whose main substrate is linoleic acid. Given the large number of carbons in a CL molecule (81 for a CL 72:8), it was not surprising to measure a natural occurrence of a few ^{13}C atoms in a non-exogenously labeled molecule (Figures 1R and S1L, untreated samples, $0 \leq M \leq 3$). Thus, we considered isotopologues with a mass of $M \geq +4$ as a cut-off for our analysis (dashed line in Figures S1L and S1M). In IL-15 wild-type (WT) CD8$^+$ T_M cells cultured with ^{13}C-glucose, almost all the newly synthesized CL contained glucose-derived carbons (Figures 1R and S1L). We next treated cells cultured in IL-15 plus ^{13}C-glucose or ^{13}C-linoleic acid for 72 h with or without AD to inhibit *de novo* CL synthesis during T_M differentiation. The data showed that both glucose- and linoleic-acid-derived ^{13}C accumulated efficiently in newly synthesized CL (Figures 1S and S1M) and revealed the differential molecular origin of carbon incorporation (Figures 1S, 1T, S1M, and S1N). When normalized to total CL, the percentage of $M \geq +4$ CL was reduced by AD only in cells cultured in ^{13}C-glucose (Figure 1T), suggesting that glucose-derived carbons are incorporated through PTPMT1-dependent *de novo* CL synthesis, whereas linoleic acid molecules are incorporated into CL through active remodeling of CL (substitution of CL acyl chains), a process not affected by AD during T_M generation (Figure S1N).

Cardiolipin Is Essential for *In Vivo* and *In Vitro* CD8$^+$ T Cell Responses

CL is synthesized in a two-step reaction in which phosphatidylglycerophosphate (PGP) is dephosphorylated by the mitochondrial phosphatase PTPMT1 into phosphatidylglycerol (PG) then fused to another diacylglycerol molecule (DAG) to generate CL by CRLS1(Zhang et al., 2011) (Figure 2A). To investigate the physiological relevance of CL in T cells, we crossed mice carrying floxed alleles of *Ptpmt1* with mice expressing CD4-Cre to selectively ablate *Ptpmt1* in T cells (*Ptpmt1*$^{flox/flox}$CD4-Cre$^-$ mice are referred to as PTPMT1 WT, *Ptpmt1*$^{flox/flox}$CD4-Cre$^+$ as PTPMT1-ΔT) (Figure 2B).

(C) Cardiolipin content in freshly isolated *Ptpmt1* WT and *Ptpmt1*$^{-/-}$ CD8$^+$ T cells.

(D) Percentage of CD8$^+$ T cells in spleens from PTPMT1 WT and PTPMT1-ΔT mice. Dots represent individual mice.

(E) PTPMT1 WT and PTPMT1-ΔT mice infected i.v. with 1×10^6 colony-forming units (CFU) LmOVA ΔActa and challenged i.v. with 5×10^7 CFU LmOVA 21 days after primary infection. Blood analyzed at indicated time.

(F) Percentage of CD8$^+$ T cells in PTPMT1 WT and PTPMT1-ΔT mice infected as in (E). Dots represent individual mice.

(G) Percentage of CD8$^+$ Tet$^+$ T cells in PTPMT1 WT and PTPMT1-ΔT mice infected as in (E). Dots represent individual mice.

(H) Bacterial burden shown as CFU per μg of liver of PTPMT1 WT and PTPMT1-ΔT mice 7 days post-LmOVA ΔActa challenge. Dots represent individual mice.

(I) T_N (CD62L^{hi}CD44^{lo}), T_E (CD62L^{lo}CD44^{hi}), and T_M (CD62L^{hi}CD44^{hi}) CD8$^+$ T cells from PTPMT1 WT and PTPMT1-ΔT mice 7 days after primary infection. Dots represent individual mice.

(J) EEC, SLEC, MPEC, and DPEC CD8$^+$ T cells from PTPMT1 WT and PTPMT1-ΔT mice 7 days after primary infection according to KLRG1 and CD127 expression. Dots represent individual mice.

(K) OCR/ECAR ratio of WT and *Ptpmt1*$^{-/-}$ CD8$^+$ T cells analyzed 7 days after secondary infection. Dots represent individual mice.

(L) *Ptpmt1* WT and *Ptpmt1*$^{-/-}$ CD8$^+$ T cells stimulated with PMA/Iono for 4 h. Also shown is the percentage of CD8$^+$ T cells producing IFN-γ and IFN-γ MFI of cytokine-producing cells.

(M) Cytoplasmic calcium levels at baseline and after αCD3 crosslinking via IgG, tapsigargin (TG), and ionomycin (iono) in *Ptpmt1* WT and *Ptpmt1*$^{-/-}$ CD8$^+$ T cells. Representative of 3 experiments.

(N) CD5, CD44, CD25, and CD69 expression in *Ptpmt1* WT and *Ptpmt1*$^{-/-}$ CD8$^+$ T cells 24 h after activation with αCD3/αCD28 + IL-2.

(O) Survival of *Ptpmt1* WT and *Ptpmt1*$^{-/-}$ CD8$^+$ T cells 24 h after activation.

(P) Cell cycle analysis assessed by FxCycle + Ki67 staining of *Ptpmt1* WT and *Ptpmt1*$^{-/-}$ CD8$^+$ T cells 24 h and 48 h after activation with αCD3/αCD28 + IL-2.

(Q) Active proliferation assessed by Ki67 expression in *Ptpmt1* WT and *Ptpmt1*$^{-/-}$ CD8$^+$ T cells 24 h and 48 h after activation with αCD3/αCD28 + IL-2.

(R) Cell proliferation assessed by CTV dilution of *Ptpmt1* WT and *Ptpmt1*$^{-/-}$ CD8$^+$ T cells 72 h after activation with αCD3/αCD28 + IL-2. Histogram representative of 4 independent experiments.

Data shown as mean ± SEM of ≥ 3 independent experiments unless indicated. Statistical comparisons for 2 groups calculated by unpaired two-tailed Student's t test, *p < 0.05; **p < 0.01; ***p < 0.001.

See also Figure S2.

Lower amount of total CL (Figure 2C) and a reduction in CL 72:8 and CL 72:6 species (Figure S2A) confirmed the effective inhibition of CL synthesis in $Ptpmt1^{-/-}$ CD8$^+$ T cells. CD8$^+$ T$_N$ cells from PTPMT1-ΔT mice showed no major differences in expression of subunits of ETC complexes, TOM20, or OPA1 in comparison with PTPMT1 WT cells (Figure S2B). PTPMT1-ΔT mice had grossly normal thymic development (Figure S2C) but peripheral lymphopenia with altered frequencies and numbers of TCRβ CD8$^+$ and CD4$^+$ (Figures 2D, S2D, and S2E) and TCRγδ CD8$^+$ and CD4$^+$ T cells (Figures S2F and S2G) in multiple organs.

To assess the effect of CL deficiency during CD8$^+$ T cell responses *in vivo*, we infected PTPMT1 WT and PTPMT-ΔT mice with a sublethal dose of attenuated *L. monocytogenes* expressing Ova (LmOVA ΔActa) and then followed the total, as well as the Ova-specific CD8$^+$ T cell response, for 3 weeks before challenging the mice with a higher dose of bacteria to evaluate recall responses and protective immunity. Although PTPMT1 WT mice mounted a primary CD8$^+$ T cell response that peaked 7 days post-infection and an enhanced secondary response after challenge, PTPMT-ΔT mice failed to do so, mounting only a very limited Ova-specific response after secondary immunization (Figures 2E–2G). This defect resulted in the persistence of bacteria in the liver of PTPMT1-ΔT mice after secondary challenge (Figure 2H). A significantly higher proportion of T$_N$ (CD62L^{hi}CD44^{lo}) compared to T$_E$ (CD62L^{lo}CD44^{hi}) cells (Figures 2I) as well as a higher proportion of early T$_E$ cells (EECs, KLRG1^{lo}CD127^{lo}) compared to short-lived T$_E$ cells (SLECs, KLRG1^{hi}CD127^{lo}) and memory precursor T$_E$ cells (MPECs, KLRG1^{lo}CD127^{hi}) (Figure 2J) was present in PTPMT1-ΔT mice 7 days post-infection, suggesting impaired T cell activation. Consistent with the role of CL in regulating cristae organization and OXPHOS efficiency, $Ptpmt1^{-/-}$ CD8$^+$ T cells isolated 7 days post-challenge exhibited a lower OCR/ECAR (oxygen consumption rate/extracellular acidification rate) ratio relative to WT counterparts (Figure 2K).

The failure of $Ptpmt1^{-/-}$ CD8$^+$ T cells to expand upon infection could be caused by defective T cell activation, a proliferative defect due to impaired mitochondrial biogenesis needed to keep up with cell division or increased cell death. We also found impaired interferon (IFN)-γ production in freshly isolated $Ptpmt1^{-/-}$ CD8$^+$ T cells (Figure 2L). This defect was not due to differential cytoplasmic calcium handling, which was grossly similar between $Ptpmt1$ WT and $Ptpmt1^{-/-}$ CD8$^+$ T cells upon T cell receptor (TCR) activation (Figure 2M). CD69, CD44, and CD25 expression 24 h after αCD3/αCD28 activation was higher in $Ptpmt1^{-/-}$ CD8$^+$ T cells (Figure 2N), corroborating the observation that the signals that drive early T cell activation were normal, at least by surface-marker expression. At the same time point, there was no sign of increased TCR stimulation-dependent apoptosis (Figure 2O). Nevertheless, CL-deficient CD8$^+$ T cells displayed a marked defect in cell cycle entry and progression at 24 h and 48 h post-activation measured by DNA content (Figure 2P) and Ki67 expression (Figure 2Q), resulting in impaired proliferation 72 h post-activation (Figure 2R). Comprehensively, these data suggest that CL is required for T cell cytokine production, cell cycle entry, and proliferation upon *in vitro* and *in vivo* antigen challenge.

Unlike CD8$^+$ IL-2 T$_E$ Cells, CD8$^+$ IL-15 T$_M$ Cells Require PTPMT1 for Survival and Cytokine Production

To assess whether the differences in activation and proliferation (Figures 2L–2R) would affect *in vitro* IL-2 T$_E$ or IL-15 T$_M$ cell differentiation, we activated $Ptpmt1$ WT and $Ptpmt1^{-/-}$ CD8$^+$ T cells for 3 days and then differentially cultured them in IL-2 or IL-15 to generate T$_E$-like cells or T$_M$-like cells, respectively. $Ptpmt1^{-/-}$ IL-15 T$_M$ cells showed a strong defect in survival (Figure S2H) and lower CD62L expression (Figure S2I) and IFN-γ production upon restimulation (Figure S2J) than did $Ptpmt1$ WT IL-15 T$_M$ cells. $Ptpmt1^{-/-}$ IL-2 T$_E$ cell properties were largely unaffected with the exception of the persistent proliferative defect (Figures S2H–S2K). Lower mitochondrial membrane potential was observed both in IL-2 T$_E$ and IL-15 T$_M$ cells (Figure S2L, upper panel), whereas mitochondrial mass was unaltered (Figure S2L, lower panel). The metabolic deficiencies in $Ptpmt1^{-/-}$ IL-15 T$_M$ cells were further highlighted by the absence of SRC (Figure S2M) and defective maximal glycolytic rate (Figure S2N).

Metabolic Reprogramming upon CD8$^+$ T Cell Activation Requires Cardiolipin, but Not Its *De Novo* Synthesis

We found that CL is necessary for CD8$^+$ T cell responses both *in vitro* and *in vivo* (Figure 2). Yet, whether CD8$^+$ T cells needed *de novo* CL synthesis early during activation was not clear. We activated WT CD8$^+$ T cells in the presence of the CL synthesis inhibitor AD during the first 48 h of stimulation, then washed out AD and differentiated the cells in IL-15 (Figure S3A). Lipidomics analysis of cells 48 h after activation, at the moment of AD wash out, showed no difference in total CL content with untreated cells (Figure S3B), although some changes were observed in the CL species profile (Figure S3C). Cells from the same experiment analyzed 3 days post-IL-15 T$_M$ differentiation showed no defects in basal or maximal respiration (Figure S3D) or IFN-γ production (Figure S3E). Then, we compared CL content of unstimulated cells with cells at different time points after αCD3/αCD28 stimulation (Figure 3A). Total CL content remained stable in the first 6 h after stimulation before strongly decreasing at later time points (Figure 3B). Of note, this drop occurred before the first cell division and without mitochondrial content dilution (Figure S3F). The drop in total CL was also paralleled by changes in acyl-chain composition (Figure 3C). CL 72:6 started to increase 24 h post-activation (Figure 3C). This observation would suggest that CL 72:6 could be the first CL species to be generated when the process of CL synthesis is re-activated, followed by CL 70:8, CL 70:6, and CL 72:9, whose increased levels are blunted by AD treatment during 48-h activation (Figures 3C and S3C). Overall, these results suggest that *de novo* synthesis of CL is not necessary for T cell priming and that its inhibition during early activation does not affect *in vitro* T$_M$ cell differentiation later on.

Even though *de novo* synthesis of CL is not necessary for T cell activation the presence of a threshold level of CL is required for *in vivo* and *in vitro* immune responses (Figure 2). Considering the metabolic reprogramming that characterizes CD8$^+$ T cells upon activation (Buck et al., 2017), we hypothesized that during antigen stimulation CL might maintain efficient mitochondrial metabolism, thus promoting proper T cell activation. To test this hypothesis, we performed experiments analyzing cytokine
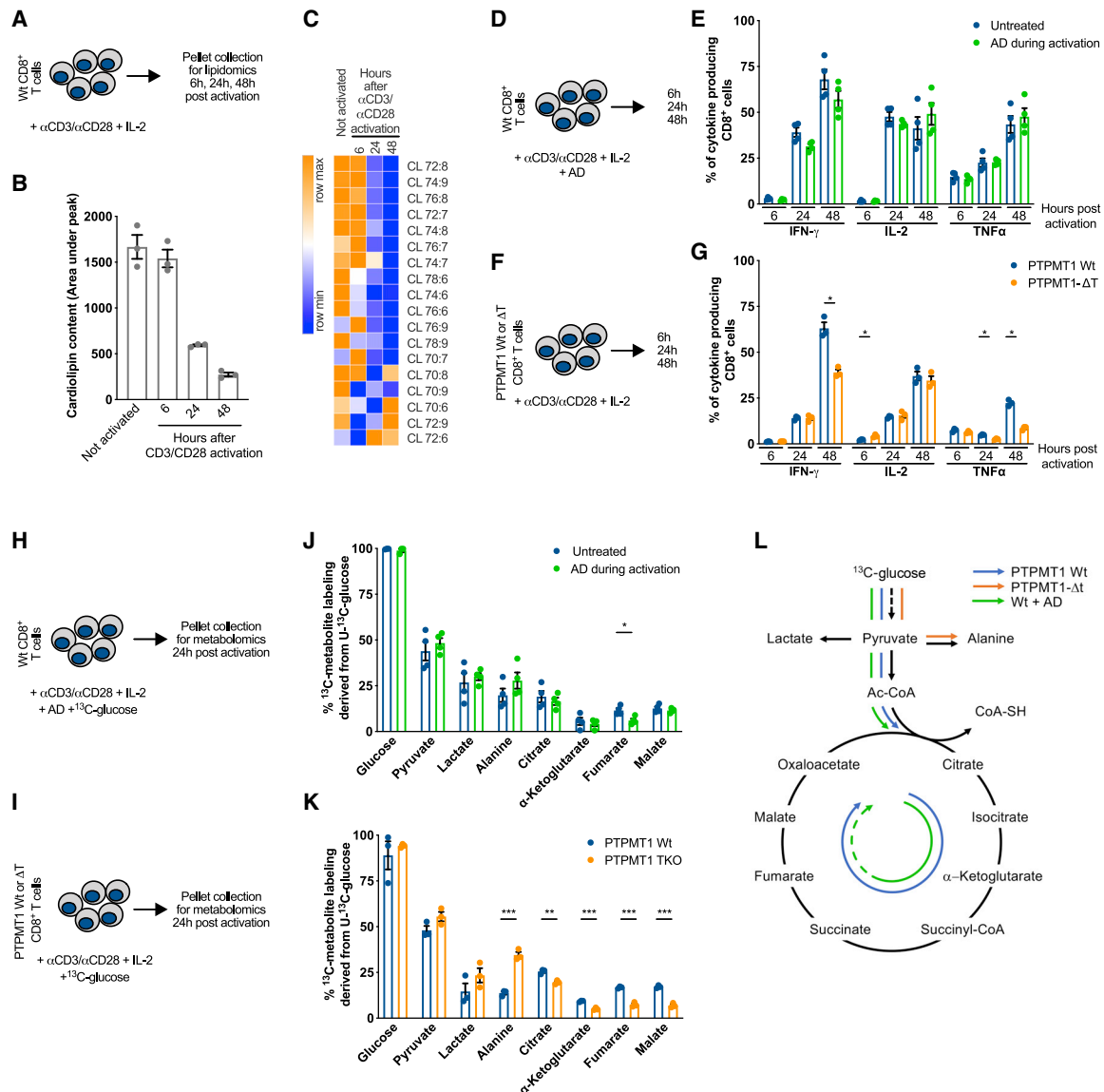
Figure 3. Metabolic Reprogramming upon CD8+ T Cell Activation Requires Cardiolipin, but Not Its *De Novo* Synthesis

(A) Schematic of CD8+ T cells activated with αCD3/αCD28 +IL-2. At indicated time points cell pellets were collected for lipidomics analysis.

(B) Total CL amount in CD8+ T cells treated as in (A)

(C) Cardiolipin species in CD8+ T cells treated as in (A).

(D) Schematic of WT CD8+ T cells activated with αCD3/αCD28 +IL-2 with ± AD.

(E) Cytokine production of WT CD8+ T cells activated as in (D) analyzed at indicated time points.

(F) Schematic of WT and *Ptpmt1*^{−/−} CD8+ T cells activated with αCD3/αCD28 + IL-2.

(G) Cytokine production of WT and *Ptpmt1*^{−/−} CD8+ T cells activated as in (F) analyzed at indicated time points.

(H) WT CD8+ T cells activated with αCD3/αCD28 + IL-2 in a medium containing 10mM ^{13}C-glucose ± AD. Twenty-four h after activation cell pellets were collected for metabolomics analysis.

(I) WT and *Ptpmt1*^{−/−} CD8+ T cells activated with αCD3/αCD28 + IL-2 in a medium containing 10mM ^{13}C-glucose. Twenty-four h after activation cell pellets were collected for metabolomics analysis.

(J) ^{13}C-glucose derived carbons incorporated into indicated metabolites in WT CD8+ T cells treated as in (H). Data represent mean ± SEM of 3 samples per genotype.

(K) ^{13}C-glucose derived carbons incorporated into indicated metabolites in *Ptpmt1* WT and *Ptpmt1*^{−/−} CD8+ T cells treated as in (I). Data represent mean ± SEM of 3 samples per genotype.

(L) Schematic of ^{13}C-glucose tracing experiment results in WT CD8+ T cells ± AD, *Ptpmt1* WT, and *Ptpmt1*^{−/−} CD8+ T cells.

Data shown as mean ± SEM of ≥ 3 independent experiments unless indicated. Statistical comparisons for 2 groups calculated by unpaired two-tailed Student's t test, *p < 0.05; **p < 0.01; ***p < 0.001.
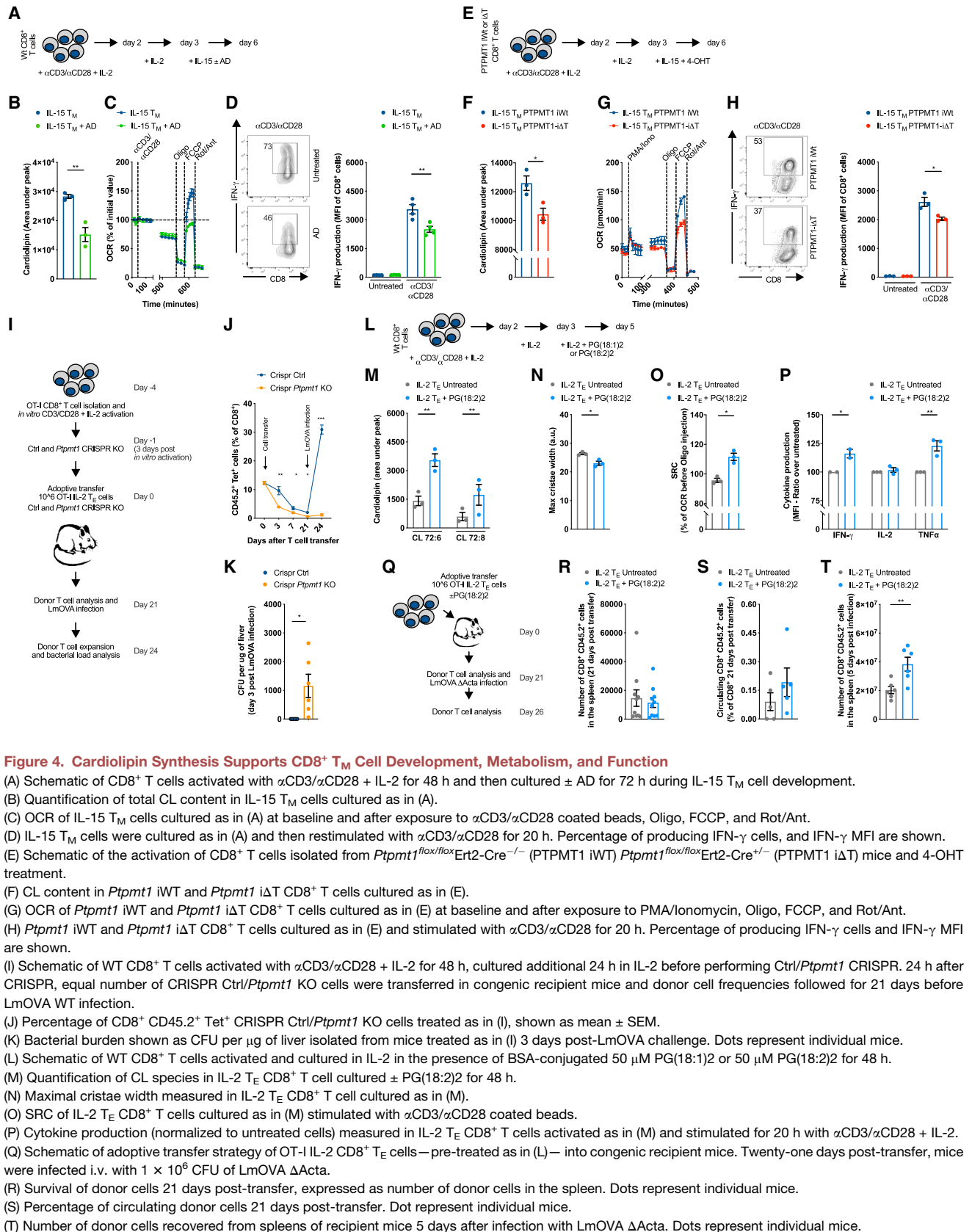
See also Figure S3.

Figure 4. Cardiolipin Synthesis Supports CD8⁺ T_M Cell Development, Metabolism, and Function

(A) Schematic of CD8⁺ T cells activated with αCD3/αCD28 + IL-2 for 48 h and then cultured ± AD for 72 h during IL-15 T_M cell development.

(B) Quantification of total CL content in IL-15 T_M cells cultured as in (A).

(C) OCR of IL-15 T_M cells cultured as in (A) at baseline and after exposure to αCD3/αCD28 coated beads, Oligo, FCCP, and Rot/Ant.

(D) IL-15 T_M cells were cultured as in (A) and then restimulated with αCD3/αCD28 for 20 h. Percentage of producing IFN-γ cells, and IFN-γ MFI are shown.

(E) Schematic of the activation of CD8⁺ T cells isolated from *Ptpmt1^flox/flox*Ert2-Cre⁻/⁻ (PTPMT1 iWT) *Ptpmt1^flox/flox*Ert2-Cre⁺/⁻ (PTPMT1 iΔT) mice and 4-OHT treatment.

(F) CL content in *Ptpmt1* iWT and *Ptpmt1* iΔT CD8⁺ T cells cultured as in (E).

(G) OCR of *Ptpmt1* iWT and *Ptpmt1* iΔT CD8⁺ T cells cultured as in (E) at baseline and after exposure to PMA/Ionomycin, Oligo, FCCP, and Rot/Ant.

(H) *Ptpmt1* iWT and *Ptpmt1* iΔT CD8⁺ T cells cultured as in (E) and stimulated with αCD3/αCD28 for 20 h. Percentage of producing IFN-γ cells and IFN-γ MFI are shown.

(I) Schematic of WT CD8⁺ T cells activated with αCD3/αCD28 + IL-2 for 48 h, cultured additional 24 h in IL-2 before performing Ctrl/*Ptpmt1* CRISPR. 24 h after CRISPR, equal number of CRISPR Ctrl/*Ptpmt1* KO cells were transferred in congenic recipient mice and donor cell frequencies followed for 21 days before LmOVA WT infection.

(J) Percentage of CD8⁺ CD45.2⁺ Tet⁺ CRISPR Ctrl/*Ptpmt1* KO cells treated as in (I), shown as mean ± SEM.

(K) Bacterial burden shown as CFU per μg of liver isolated from mice treated as in (I) 3 days post-LmOVA challenge. Dots represent individual mice.

(L) Schematic of WT CD8⁺ T cells activated and cultured in IL-2 in the presence of BSA-conjugated 50 μM PG(18:1)2 or 50 μM PG(18:2)2 for 48 h.

(M) Quantification of CL species in IL-2 T_E CD8⁺ T cell cultured ± PG(18:2)2 for 48 h.

(N) Maximal cristae width measured in IL-2 T_E CD8⁺ T cell cultured as in (M).

(O) SRC of IL-2 T_E CD8⁺ T cells cultured as in (M) stimulated with αCD3/αCD28 coated beads.

(P) Cytokine production (normalized to untreated cells) measured in IL-2 T_E CD8⁺ T cells activated as in (M) and stimulated for 20 h with αCD3/αCD28 + IL-2.

(Q) Schematic of adoptive transfer strategy of OT-I IL-2 CD8⁺ T_E cells—pre-treated as in (L)— into congenic recipient mice. Twenty-one days post-transfer, mice were infected i.v. with 1 × 10⁶ CFU of LmOVA ΔActa.

(R) Survival of donor cells 21 days post-transfer, expressed as number of donor cells in the spleen. Dots represent individual mice.

(S) Percentage of circulating donor cells 21 days post-transfer. Dot represent individual mice.

(T) Number of donor cells recovered from spleens of recipient mice 5 days after infection with LmOVA ΔActa. Dots represent individual mice.

production and metabolic properties of WT CD8^{+} T cells cultured with or without AD during activation, as well as of *Ptpmt1* WT and *Ptpmt1*^{−/−} CD8^{+} T cells. WT cells were fully equipped with CL, and only *de novo* synthesis was pharmacologically inhibited. In *Ptpmt1*^{−/−} CD8^{+} T cells, as a result of lacking PTPMT1 and *de novo* CL synthesis, the cells were CL deficient. Cytokine production was tested at different time points post-activation (6 h, 24 h, and 48 h) (Figure 3D). Although pharmacological inhibition of PTPMT1 by AD did not affect cytokine production (Figures 3D and 3E), *Ptpmt1*^{−/−} CD8^{+} T cells showed a marked reduction in IFN-γ and tumor necrosis factor (TNF) production with unaltered IL-2 synthesis (Figures 3F and 3G). Then, we traced ^{13}C-glucose during the first 24 h post-αCD3/αCD28 stimulation in WT CD8^{+} T cells cultured with or without AD and in *Ptpmt1* WT and *Ptpmt1*^{−/−} CD8^{+} T cells (Figures 3H and 3I). Both WT CD8^{+} T cells incubated with or without AD (Figures 3J and S1G–S1I) and *Ptpmt1* WT and *Ptpmt1*^{−/−} T cells (Figures 3K and S3L–S3N) acquired glucose equally and then metabolized it to pyruvate and lactate to the same extent. However, although pyruvate entered the tricarboxylic acid (TCA) cycle and ^{13}C carbons were incorporated into TCA cycle intermediates in both in WT CD8^{+} T cells incubated with or without AD (Figures 3J, S1J, and S1K) as well as in *Ptpmt1* WT control CD8^{+} T cells (Figures 3K, S3O, and S3P), it was preferentially shunted to alanine with decreased incorporation into TCA cycle intermediates in *Ptpmt1*^{−/−} T cells (Figure 3L). Consistent with the role of PTPMT1 in modulating SDH function (Nath et al., 2015), AD-treated WT cells had lower levels of ^{13}C-glucose-derived carbon incorporation into fumarate (Figure 3J). These results highlight that CD8^{+} T cells require basal levels of CL, but not its *de novo* synthesis, to allow metabolic activation upon TCR triggering.

Cardiolipin Synthesis Supports CD8^{+} T_M Cell Development, Metabolism, and Function

PTPMT1-ΔT mice allowed us to investigate the role of *de novo* CL synthesis in T cell responses *in vivo*. However, this mouse model produced T cells deficient for *Ptpmt1* from embryonic development and therefore did not allow us to test the role of *de novo* CL synthesis exclusively in T_M development. We tackled this question from multiple angles by using pharmacological inhibition (Figure 4A), inducible genetic deletion (Figures 4E), and a CRISPR approach (Figure 4I). Inhibition of PTPMT1 with AD during IL-15 T_M differentiation (Figure 4A) reduced total CL content (Figure 4B) by additive reduction of the most abundant CL species in CD8^{+} T cells (Figure S4A). AD worked selectively on CL, because variations in other lipids were limited (Figure S4A). CL synthesis is a slow process, and IL-15 T_M cells did not show alterations in OCR upon direct AD treatment (Figure S4B). Mitochondrial mass (Figure S4C, left panel) or ETC complex levels were not altered (Figure S4C, right panel), although AD treatment induced accumulation of short forms of OPA1 (Figure S4C, right panel), commonly observed during mitochondrial fission (Ban et al., 2017; Cipolat et al., 2006; Cogliati et al., 2013). We previously described how T_M cells have tight cristae with closely associated ETC complexes, which

renders their mitochondrial membranes less susceptible to digitonin disruption than those of T_E cells (Buck et al., 2016). Hypothesizing that CL might play a key role in this process, we performed a similar experiment where untreated or AD-treated IL-15 T_M cells were incubated with increasing concentrations of digitonin followed by separation of the crude membrane-bound fraction from solubilized proteins by centrifugation. We found a greater proportion of ETC complex subunits in the soluble fraction of AD-treated cells (Figure S4D), indicating that ETC complexes were more loosely embedded in the IMM or that the protein/lipid ratio was altered, because the membranes were more susceptible to digitonin disruption when CL synthesis was inhibited. Electron micrographs of untreated and AD-treated IL-15 T_M cells further confirmed cristae structure alterations with increased maximal cristae width (Figure S4E), and live-cell imaging revealed mitochondrial fragmentation (Figure S4F) upon CL synthesis inhibition. *In vitro* IL-15 T_M rely on OXPHOS to meet their energetic needs (Buck et al., 2017). In line with this, only IL-15 T_M cells exhibited a survival defect when CL synthesis was inhibited (Figure S4G). Furthermore, AD treatment impaired CD62L expression (Figure S4H), SRC (Figure 4C), and IFN-γ production (Figure 4D) in IL-15 T_M cells.

Although our data showed that AD selectively inhibited CL synthesis (Figures 4B and S4A) to rule out the possibility of off-target effects of the drug we crossed a tamoxifen (4-OHT) inducible (Ert2-CRE) mouse to the *Ptpmt1*[flox/flox] mouse to generate a strain (*Ptpmt1* iΔT) whose cells could be inducibly deleted of *Ptpmt1* upon exposure to 4-OHT *in vitro*. To avoid any effect on activation and early differentiation, we induced *Ptpmt1* deletion *in vitro* only during T_M cell differentiation in IL-15 (Figures 4E and S4I), without a reduction in *Crls1* and *Tafazzin* (*Taz*) expression levels (Figure S4I). *Ptpmt1* iΔT cells recapitulated results from AD-treated cells showing lower CL content than in *Ptpmt1*[flox/flox]Ert2-Cre[−] (*Ptpmt1* iWT) T cells subjected to the same 4-OHT treatment (Figure 4F). IL-15 *Ptpmt1* iΔT cells also showed a survival defect and a lower CD62L expression (Figures S4J), SRC (Figure 4G), and IFN-γ production (Figure 4H) than did *Ptpmt1* iWT T cells (Figure S4K).

Finally, to test the role of PTPMT1 *in vivo* during T_M cell generation, we used a CRISPR approach. We activated OT-I cells *in vitro* and deleted *Ptpmt1* only at the peak of effector phase (3 days post-activation), which allowed normal T cell activation and expansion prior to deleting *Ptpmt1*. After an additional 24 h, we transferred an equal number of CRISPR Ctrl and CRISPR *Ptpmt1* knockout (KO) cells into congenic mice and tracked donor cells for 21 days before LmOVA infection (Figure 4I). CRISPR *Ptpmt1* KO cells exhibited lower survival *in vivo* during the T_E cell contraction phase (Figure 4J). Strikingly, when mice were then infected with LmOVA, only CRISPR Ctrl cells expanded, whereas CRISPR *Ptpmt1* KO cells failed to do so (Figure 4J). As a result, only CRISPR Ctrl cells were able to efficiently clear bacteria from the liver of infected mice (Figure 4K). In summary, PTPMT1 and CL synthesis support CD8^{+} T_M cell generation both *in vitro* and *in vivo*.

Data shown as mean ± SEM of ≥3 independent experiments unless indicated. Statistical comparisons for 2 groups calculated by unpaired two-tailed Student's t test, $*p < 0.05$; $**p < 0.01$; $***p < 0.001$.
See also Figure S4.

Enhancing Cardiolipin Synthesis Promotes the Generation of Memory-like CD8+ T Cells

T cells with elongated mitochondria and tight cristae are more fit in adoptive cellular immunotherapy models in mice (Buck et al., 2016). We asked whether increasing CL content, which could promote cristae tightness, would also have a similar effect on T cell fitness. To increase CL content we supplemented IL-2 T_E and IL-15 T_M cells with different forms of the CL precursor phosphatidylglycerol (PG), i.e., PG(18:2)2 and PG(18:1 Δ9-*cis*)2, for 48 h (Figure 4L). We found that, without affecting the overall lipidome (Figure S4L), only PG(18:2)2 increased total CL content as well as CL 72:6 and CL 72:8 in both IL-2 T_E and IL-15 T_M cells (Figures 4M and S4M–S4O). PG(18:1)2 did not increase total CL or the main CL forms containing oleic acid CL 72:4, Cl 72:5, and CL 70:4 (data not shown). The higher CL content observed in IL-2 T_E cells, although not sufficient to counteract mitochondrial fragmentation (Figure S4P), tightened cristae (Figures 4N and S4Q) and resulted in higher SRC (Figure 4O), and increased IFN-γ, TNF production (Figure 4P), and expression of CD25 and CD62L (Figure S4R). The further increase in CL content in IL-15 T_M cells mediated by PG(18:2)2 (Figure S4M) did not induce changes in surface marker expression (Figure S4R), SRC (Figure S4S), or cytokine production (Figure S4T), suggesting the existence of a maximal threshold for CL content to modulate T cell function. To investigate whether these observations held true *in vivo*, we adoptively transferred untreated and PG(18:2)2-treated OT-I IL-2 T_E cells into congenic mice and tracked cell survival and responses against LmOVA ΔActa infection (Figure 4Q). There were no differences in the number of donor cells in the spleen (Figure 4R), with only a trend toward more circulating PG(18:2)2-treated cells 21 days post-cell transfer (Figure 4S), suggesting no difference in long-term survival between the two populations. However, 5 days after LmOVA ΔActa infection, a greater number of PG(18:2)2-treated cells were recovered in the spleen of infected mice (Figure 4T). These data raise the possibility that higher CL content protects cristae structure upon restimulation, limiting cytochrome *c* release and activation-induced cell death (AICD) (Corrado et al., 2016). Of note, PG(18:2)2 supplementation in the context of 4-OHT-induced deletion of *Ptpmt1* in IL-15 T_M cells (Figure S4U) did not rescue CL content (Figure S4V), survival (Figure S4W), or cytokine production (Figure S4X), likely reflecting inefficient incorporation of external PG into CL in the absence of PTPMT1 (Serricchio et al., 2018). Collectively, these data show that enhancing CL content *in vitro* and *in vivo* generates T cells that are metabolically and functionally fit.

CD8+ T Cell Defects Observed in TAZ KO Mice Are Not Intrinsic to CD8+ T Cells

Given the functions of CL in CD8+ T cell biology outlined here, we set out to investigate the role of *Tafazzin* in T cells in a mouse model of Barth syndrome and in a small cohort of Barth syndrome patients. We analyzed CL content in CD8+ T cells isolated from *Tafazzin* KO mice (full-body deletion) (Figure 5A) at 20 weeks of age, when cardiomyopathy and muscle weakness start to develop (Cadalbert et al., 2015). CL deficiency was not only limited to muscles but also observed in CD8+ T cells of *Tafazzin* KO mice (Figures 5B and 5C) together with a slight but significant reduction in CD62L^{hi}CD44^{hi} T_{CM} cells (Figure 5D). Upon *in vitro*

stimulation, *Tafazzin* KO CD8+ T cells produced less IFN-γ (Figures 5E–5G) and proliferated less efficiently (Figure 5H). In addition, IL-15 T_M CD8+ *Tafazzin* KO cells showed an accumulation of short forms of OPA1, a reduction in CIII protein levels (Figure S5A), and altered expression of CD25 and CD62L (Figure S5B) in comparison with IL-2 T_E cells.

To understand whether the T cell impairment observed in mice with total body deletion of *Tafazzin* was CD8+ T cell intrinsic, we generated *Taz* CRISPR KO OT-I cells and investigated, *in vitro* and *in vivo*, the result of TAZ acute deletion on T cell activation, expansion, and response to infection (Figure S5C). The absence of TAFAZZIN (Figures S5D and S5E) did not change the overall lipid profile (Figure S5F), CL amount (Figure S5G), or composition (Figure S5H) comparable to those of Ctrl CRISPR T cells 6 h post-activation *in vitro*, the same time point when we observed alterations in CLs in WT cells (Figure 3C), as well as the activation-induced expression of CD5, CD25, CD44, and CD69 (Figure S5I). Thus, TAFAZZIN was dispensable for CD8+ T cell activation. To translate these observations *in vivo*, we adoptively transferred Ctrl and *Taz* CRISPR KO OT-I cells into recipient mice and followed their response to LmOVA infection (Figure S5J). Despite *Taz* CRISPR KO CD8+ T cells showing a defective switch from EEC to SLEC (Figures S5K and S5L) (both after primary and secondary challenge), similar to what observed in PTPMT1-ΔT mice (Figure 2J), CD62L and CD44 expression was similar (Figure S5M). Moreover, *Taz* CRISPR KO cells responded to antigen stimulation similarly to Ctrl cells and generated T_M cells that efficiently expanded upon secondary infection (Figure S5J). As per TAZ function, 7 days post-secondary infection-sorted CD8+ OT-I *Taz* CRISPR KO OT-I cells showed a reduced level of CL in comparison with WT cells (Figures S5N and S5O). Nevertheless, even increasing the window between primary and secondary LmOVA challenge from 3 weeks to 2 months did not alter CD8+ T cell function but confirmed defects in the EEC to SLEC transition (Figures S5Q–S5T). In both experiments, Taz CRISPR KO CD8+ T cells cleared bacteria from the liver of infected mice (Figures S5P and S5U). Overall, these data suggest that the defects observed in the T cell compartment of TAZ KO mice either are not CD8+ T cell intrinsic or might derive from hematopoietic lineage developmental alterations.

T Cell Defects in a Small Cohort of Barth Syndrome Patients

We analyzed peripheral blood mononuclear cells (PBMCs) from 5 patients under the care of the NHS Barth syndrome Service (Barth syndrome group average age 13 years, min 6 years, max 28 years; healthy donor group average age 28 years, min 22 years, max 39 years) with pathology confirmed both by MLCL/CL(18:2)4 ratio (Figure 5I) and *TAFAZZIN* sequencing (data not shown). Patients that had undergone cardiac transplantation, and hence were on immunosuppressive drugs, were excluded from the analysis. We found that patients had significantly lower relative frequencies of CD8+ T cells in PBMCs than did healthy donors (Figure 5J), with no apparent differences in the CD4+ T cell compartment (Figure S5V). Although no differences were detected in the expression of naive/memory CD45RA and CD45RO (Figure S5W), nor in surface markers of different CD8+ T_M subpopulations (Figure S5X), CD8+ T cells
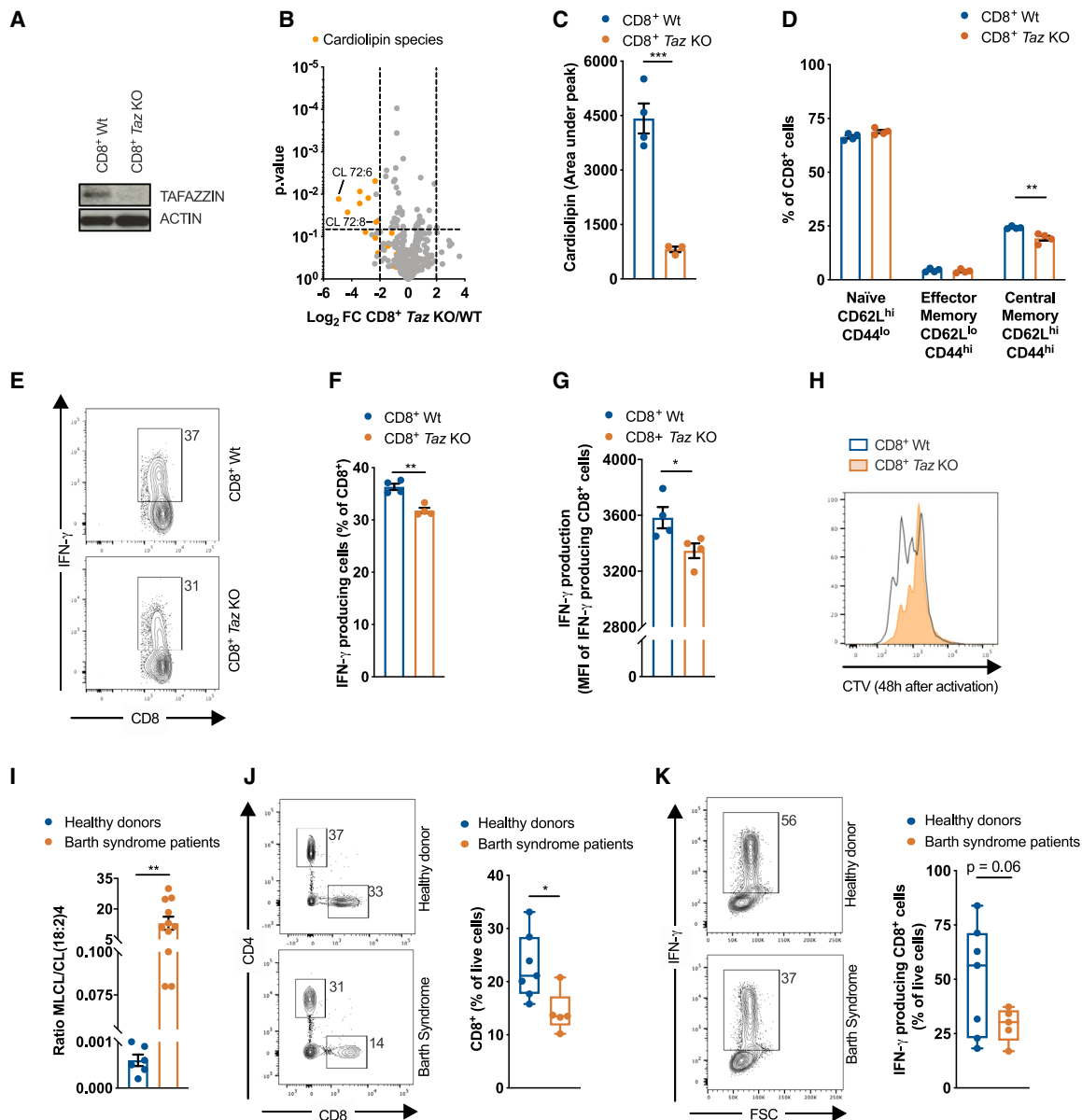
Figure 5. CD8+ T Cell Defects n *Tafazzin*-Deficient Mice and in a Small Cohort of Barth Syndrome Patients

(A) Immunoblot analysis of cell extracts from freshly isolated WT and *Tafazzin* KO CD8+ T cells.

(B) Lipids extracted from freshly isolated CD8+ T cells from 20-week old WT and *Tafazzin* KO. Data show Log2FC and p value calculated with ANOVA test.

(C) Total CL amount in freshly isolated CD8+ T cells from 20-week old WT and *Tafazzin* KO mice. Dots represent individual mice.

(D) T_N (CD62L^{hi}CD44^{lo}), T_{EM} (CD62L^{lo}CD44^{hi}), and T_{CM} (CD62L^{hi}CD44^{hi}) CD8+ T cells from 20-week–old WT and *Tafazzin* KO mice. Dots represent individual mice.

(E–G) Representative flow cytometry analysis (E), percentage of IFNγ producing CD8+ T cells (F), and IFN-γ MFI of CD8+ IFN-γ+ T cells (G) of freshly isolated CD8+ T cells from 20-weeks old WT and *Tafazzin* KO mice stimulated for 4 h with PMA/iono. Dots represents individual mice.

(H) Cell proliferation of CD8+ T cells from 20-week-old WT and *Tafazzin* KO mice 48 h after activation with αCD3/αCD28 + IL-2. Dots represent individual mice.

(I) Monolysocardiolipin/cardiolipin (18:2)4 ratio in healthy donors and Barth syndrome patients. Dots represent individual donors.

(J) Representative flow cytometry analysis and quantification of the percentage of CD8+ T cells in hPBMCs from healthy donors and Barth syndrome patients. Dots represent individual donors.

(K) Representative flow cytometry analysis and quantification of IFN-γ production of CD8+ T cells from healthy donors and Barth syndrome patients activated with PMA/iono for 5 h. Dots represent individual donors.

Data shown as mean ± SEM of ≥3 independent experiments unless indicated. Statistical comparisons for two groups calculated by unpaired two-tailed Student's t test or Anova test, where indicated, *p < 0.05; **p < 0.01; ***p < 0.001.

See also Figure S5.

from Barth syndrome patients showed a trend toward impaired IFN-γ production after stimulation (Figure 5K). Overall, our analysis suggests a possible CD8$^+$ T cell impairment in patients affected by Barth syndrome.

DISCUSSION

Although metabolic reprogramming during the adaptive immune response has been widely explored in recent years, the role of mitochondrial lipid composition and, in particular, CL in this scenario remained uninvestigated. Our study shows that the dynamic regulation of synthesis and remodeling of a single lipid confers to T cell mitochondria the plasticity necessary for adapting to the different metabolic and functional requirements during all phases of the T cell response—from activation, to expansion, contraction, and eventually long-term immune protection.

In the absence of CL, PTPMT1-ΔT mice mounted a defective CD8$^+$ T cell response upon infection. We found that *de novo* CL synthesis was not necessary for T cell activation, but the presence of a sufficient initial pool of CL in the mitochondrial membrane was required. Indeed, *ex vivo*-activated *Ptpmt1*$^{-/-}$ CD8$^+$ T cells were defective in cytokine production and metabolic adaptation even before a proliferative defect emerged. During activation the CL profile is modulated in human T cells (Mürke et al., 2016), whereas in murine CD4$^+$ T cells stomatin-like protein 2 (SLP2) organizes CL in lipid rafts (Christie et al., 2012). Given the interaction of CL with different subunits of the ETC, and the burst in ROS during T cell activation (Dudek, 2017; Sena et al., 2013), it is tempting to speculate that CL modifications/oxidations are required for the metabolic shifts that occur during early T cell activation and that *Ptpmt1* ablation might alter ROS production upon TCR triggering. It also remains to be determined whether during antigen stimulation ROS causes CL oxidation to instruct mitochondrial structural and metabolic reprograming or whether ROS acts in a CL-independent manner.

Our lab previously showed that *Opa1*-deficient T cells are able to form T$_E$ cells after primary infection with a later failure in T$_M$ cell generation (Buck et al., 2016). Here, we characterize how *Ptpmt1*$^{-/-}$ T cells have a broader defective phenotype, failing to activate properly and expand into T$_E$ cells. Thus, whereas OPA1 and CL might in part functionally share the role of maintaining cristae structure, the different nature of a protein versus a lipid, a specific signaling role for CL during T cell activation, and a more structural requirement for CL synthesis for mitochondrial biogenesis during T cell expansion might contribute to the differential cellular behavior of the two models.

When autophagy is triggered by low nutrient availability, mitochondria elongate to sustain viability and avoid starvation-induced cell death (Buck et al., 2016; Gomes et al., 2011). This change is accompanied by an increase in the number of cristae, assembly of respiratory chain supercomplexes, and in the dimerization and activity of the ATP synthase (Balsa et al., 2019; Gomes et al., 2011). Here we show that upon glucose restriction, cellular metabolism rapidly responds by synthesizing CL, independently from changes in mitochondrial mass, thus increasing SRC and limiting apoptosis. Of note, both these pro-survival features are lost if *de novo* CL synthesis is inhibited during glucose restriction. CL binds selectively but transiently to the ATP syn-

thase, affecting its supramolecular organization (Acehan et al., 2011; Duncan et al., 2016; Mehdipour and Hummer, 2016), as well as to complex I (Jussupow et al., 2019) and complex II (Schwall et al., 2012), modulating their stability and function. Of note, in our experiments the subunit levels of complex I and complex II (NDUFB8 and SDHB, respectively) are modulated together with CL during glucose restriction, or upon CD28 co-stimulation, which also results in increased OXPHOS efficiency and higher CL content.

Safeguarding mitochondrial integrity and metabolism is instrumental in generating long-lived and fit T$_M$ cells (Buck et al., 2016). Indeed, mitochondrial fusion-fission cycles allow the segregation and elimination of dysfunctional mitochondria through autophagy (Pickles et al., 2018). Induction of autophagy sustains T$_M$ cell development, whereas its inhibition combined with mitochondrial dysfunction contributes to AICD of short-lived T$_E$ cells (Corrado et al., 2016; Puleston et al., 2014; Xu et al., 2014). We show that *de novo* CL synthesis is required to increase mitochondrial metabolic capacity and allow AICD resistance during T$_M$ cell differentiation. Thus, increasing CL content might improve adoptive cellular immunotherapy, where a lack of T cell persistence after transfer remains an issue (Restifo et al., 2012; Tschumi et al., 2018).

Mutations in *TAFAZZIN* responsible for Barth syndrome alter CL remodeling and reduce total CL content over time due to the inability of cells to regenerate mature CL from MLCL (Schlame et al., 2003). In the mouse gut, intraepithelial lymphocytes (IELs) maintain a controlled activation state that relies on mitochondria through a TAFAZZIN-dependent CL remodeling mechanism (Konjar et al., 2018). Although able to migrate to the site of infection and produce cytokines, bone marrow chimera-derived *Tafazzin*-deficient IELs are not able to restrict *E. vermiformis* infection (Konjar et al., 2018). Here, we reinforce these observations in a total body *Tafazzin* KO mouse model, resembling more closely the human pathology where *TAFAZZIN* inactivating mutations are not confined to the hematopoietic compartment. In particular, experiments in TAZ KO mice suggested that reduced number and impaired function of CD8$^+$ T cells follow long-term systemic CL deficiency. In addition, our CRISPR data support the idea that the T cell functional defects observed in bone marrow chimera *Tafazzin*-deficient mice, as well as in total body TAZ KO mice, might not be CD8$^+$ T cell intrinsic or might derive from hematopoietic lineage developmental alterations.

Cardiomyopathy and neutropenia are life-threatening features of Barth syndrome. Some Barth syndrome patients require cardiac transplantation followed by lifelong immunosuppressive drug treatment (Mangat et al., 2007). Our analysis of hPBMCs from a limited number of Barth syndrome patients suggests the possibility of a relative lymphopenia and functional impairment in the CD8$^+$ T cell compartment. However, more detailed clinical studies to assess the absolute number, frequency, and function of lymphocyte subsets in a larger number of patients are required. Less efficient responses to T cell-mediated vaccines or lower susceptibility to acute organ rejection after heart transplant in Barth syndrome patients compared to non-affected age-matched individuals might be expected if our hypothesis holds true. In our view it is possible that the adaptive immune phenotype in these patients might exacerbate the impact of

neutropenia in the susceptibility to infections by a combination of the impaired activation, proliferation, and differentiation of T_M cells.

In conclusion, we describe the pivotal role of the dynamic regulation of CL synthesis in modulating CD8$^+$ T cell function during the immune response, from activation to T_M cell differentiation. Absence of CL due to impaired synthesis (PTPMT1-ΔT) or remodeling (*Tafazzin* KO) results in compromised CD8$^+$ T cell function, although our data suggest the latter is not CD8$^+$ T cell intrinsic. Moreover, we propose modulation of CL content and/or composition as a strategy to improve adoptive cell immunotherapy. Lastly, our findings suggest a potentially unrecognized T cell impairment in Barth syndrome patients, broadening the spectrum of pathologic features of Barth syndrome and prompting a further evaluation of immune function in patients and in clinical trials targeting CL modifications.

Limitations of study

Although our study shows that cardiolipin synthesis is regulated during CD8$^+$ T cell responses to infection, it addresses neither the role of different CL species nor the regulation of acyl chain modifications. It also remains to be determined the role of cardiolipin oxidation and its interplay with ROS production upon CD8$^+$ T cell activation. Lastly, analysis of T cell function in larger cohort of Barth syndrome patients and epidemiological studies on susceptibility to acute organ rejection after heart transplant are necessary to further corroborate our observations.

STAR★METHODS

Detailed methods are provided in the online version of this paper and include the following:

- KEY RESOURCE TABLE
- RESOURCE AVAILABILITY
  - ○ Lead Contact
  - ○ Materials Availability
  - ○ Data and Code Availability
- EXPERIMENTAL MODEL AND SUBJECT DETAILS
  - ○ Cell Culture and Drug Treatment
  - ○ Mice and Immunizations
- METHODS DETAILS
  - ○ Bacterial Burden
  - ○ Adoptive Transfers
  - ○ Flow Cytometry
  - ○ Confocal and Electron Microscopy Imaging
  - ○ Metabolic Phenotyping
  - ○ Lipid Extraction and Quantification
  - ○ Glucose and Linoleic Acid Tracing into Cardiolipin
  - ○ Glucose Tracing into Central Carbon Metabolites
  - ○ RT-PCR
  - ○ mtDNA/nDNA Quantification
  - ○ Calcium Flux
  - ○ Cell Cycle Analysis
  - ○ Western Blotting
  - ○ *Generation of CRISPR KO* T Cells
- QUANTIFICATION AND STATISTICAL ANALYSIS

AUTHOR CONTRIBUTIONS

M.C. and E.L.P. designed research. M.C., J.H.E., M.V., B.A., C.G.S., D.S., E.T., D.O., E.J.P., and E.L.P. provided conceptual input. M.C., J.H.E., M.V., L.J.F., D.E.S., M.J., F.B., M.S., E.A., M.A., A.Q., J.D.C., T.C., K.M.G., A.M.K., R.K., A.E.P., and R.K.G. performed experiments and analyzed data. M.C. and E.L.P. wrote the manuscript.

DECLARATION OF INTERESTS

E.L.P. is a SAB member of Immunomet, and E.L.P. and E.J.P. are founders of Rheos Medicines. E.L.P. is Advisory Board member of Cell and Cell Metabolism.

REFERENCES

Acehan, D., Malhotra, A., Xu, Y., Ren, M., Stokes, D.L., and Schlame, M. (2011). Cardiolipin affects the supramolecular organization of ATP synthase in mitochondria. Biophys. J. *100*, 2184–2192.

Bailis, W., Shyer, J.A., Zhao, J., Canaveras, J.C.G., Al Khazal, F.J., Qu, R., Steach, H.R., Bielecki, P., Khan, O., Jackson, R., et al. (2019). Distinct modes of mitochondrial metabolism uncouple T cell differentiation and function. Nature *571*, 403–407.

Balsa, E., Soustek, M.S., Thomas, A., Cogliati, S., García-Poyatos, C., Martín-García, E., Jedrychowski, M., Gygi, S.P., Enriquez, J.A., and Puigserver, P. (2019). ER and Nutrient Stress Promote Assembly of Respiratory Chain Supercomplexes through the PERK-elF2α Axis. Mol. Cell *74*, 877–890.e6, e876.

Ban, T., Ishihara, T., Kohno, H., Saita, S., Ichimura, A., Maenaka, K., Oka, T., Mihara, K., and Ishihara, N. (2017). Molecular basis of selective mitochondrial fusion by heterotypic action between OPA1 and cardiolipin. Nat. Cell Biol. *19*, 856–863.

Barth, P.G., Scholte, H.R., Berden, J.A., Van der Klei-Van Moorsel, J.M., Luyt-Houwen, I.E., Van 't Veer-Korthof, E.T., Van der Harten, J.J., and Sobotka-Plojhar, M.A. (1983). An X-linked mitochondrial disease affecting cardiac muscle, skeletal muscle and neutrophil leucocytes. J. Neurol. Sci. *62*, 327–355.

Bione, S., D'Adamo, P., Maestrini, E., Gedeon, A.K., Bolhuis, P.A., and Toniolo, D. (1996). A novel X-linked gene, G4.5. is responsible for Barth syndrome. Nat. Genet. *12*, 385–389.

Buck, M.D., O'Sullivan, D., Klein Geltink, R.I., Curtis, J.D., Chang, C.H., Sanin, D.E., Qiu, J., Kretz, O., Braas, D., van der Windt, G.J., et al. (2016). Mitochondrial Dynamics Controls T Cell Fate through Metabolic Programming. Cell *166*, 63–76.

Buck, M.D., Sowell, R.T., Kaech, S.M., and Pearce, E.L. (2017). Metabolic Instruction of Immunity. Cell *169*, 570–586.

Cadalbert, L.C., Ghaffar, F.N., Stevenson, D., Bryson, S., Vaz, F.M., Gottlieb, E., and Strathdee, D. (2015). Mouse Tafazzin Is Required for Male Germ Cell Meiosis and Spermatogenesis. PLoS One *10*, e0131066.

Chan, D.C. (2020). Mitochondrial Dynamics and Its Involvement in Disease. Annu. Rev. Pathol. *15*, 235–259.

Chang, C.H., Curtis, J.D., Maggi, L.B., Jr., Faubert, B., Villarino, A.V., O'Sullivan, D., Huang, S.C., van der Windt, G.J., Blagih, J., Qiu, J., et al. (2013). Posttranscriptional control of T cell effector function by aerobic glycolysis. Cell *153*, 1239–1251.

Christie, D.A., Mitsopoulos, P., Blagih, J., Dunn, S.D., St-Pierre, J., Jones, R.G., Hatch, G.M., and Madrenas, J. (2012). Stomatin-like protein 2 deficiency in T cells is associated with altered mitochondrial respiration and defective CD4+ T cell responses. J. Immunol. *189*, 4349–4360.

Cipolat, S., Martins de Brito, O., Dal Zilio, B., and Scorrano, L. (2004). OPA1 requires mitofusin 1 to promote mitochondrial fusion. Proc. Natl. Acad. Sci. USA *101*, 15927–15932.

Cipolat, S., Rudka, T., Hartmann, D., Costa, V., Serneels, L., Craessaerts, K., Metzger, K., Frezza, C., Annaert, W., D'Adamio, L., et al. (2006). Mitochondrial rhomboid PARL regulates cytochrome c release during apoptosis via OPA1-dependent cristae remodeling. Cell *126*, 163–175.

Clarke, S.L., Bowron, A., Gonzalez, I.L., Groves, S.J., Newbury-Ecob, R., Clayton, N., Martin, R.P., Tsai-Goodman, B., Garratt, V., Ashworth, M., et al. (2013). Barth syndrome. Orphanet J. Rare Dis. *8*, 23.

Cogliati, S., Frezza, C., Soriano, M.E., Varanita, T., Quintana-Cabrera, R., Corrado, M., Cipolat, S., Costa, V., Casarin, A., Gomes, L.C., et al. (2013). Mitochondrial cristae shape determines respiratory chain supercomplexes assembly and respiratory efficiency. Cell *155*, 160–171.

Corrado, M., Mariotti, F.R., Trapani, L., Taraborrelli, L., Nazio, F., Cianfanelli, V., Soriano, M.E., Schrepfer, E., Cecconi, F., Scorrano, L., and Campello, S. (2016). Macroautophagy inhibition maintains fragmented mitochondria to foster T cell receptor-dependent apoptosis. EMBO J. *35*, 1793–1809.

Dudek, J. (2017). Role of Cardiolipin in Mitochondrial Signaling Pathways. Front. Cell Dev. Biol. *5*, 90.

Dudek, J., Hartmann, M., and Rehling, P. (2019). The role of mitochondrial cardiolipin in heart function and its implication in cardiac disease. Biochim. Biophys. Acta Mol. Basis Dis. *1865*, 810–821.

Duncan, A.L., Robinson, A.J., and Walker, J.E. (2016). Cardiolipin binds selectively but transiently to conserved lysine residues in the rotor of metazoan ATP synthases. Proc. Natl. Acad. Sci. USA *113*, 8687–8692.

Frey, T.G., and Mannella, C.A. (2000). The internal structure of mitochondria. Trends Biochem. Sci. *25*, 319–324.

Frezza, C., Cipolat, S., Martins de Brito, O., Micaroni, M., Beznoussenko, G.V., Rudka, T., Bartoli, D., Polishuck, R.S., Danial, N.N., De Strooper, B., and Scorrano, L. (2006). OPA1 controls apoptotic cristae remodeling independently from mitochondrial fusion. Cell *126*, 177–189.

Geltink, R.I.K., Kyle, R.L., and Pearce, E.L. (2018). Unraveling the Complex Interplay Between T Cell Metabolism and Function. Annu. Rev. Immunol. *36*, 461–488.

Gomes, L.C., Di Benedetto, G., and Scorrano, L. (2011). During autophagy mitochondria elongate, are spared from degradation and sustain cell viability. Nat. Cell Biol. *13*, 589–598.

Gonzalvez, F., Schug, Z.T., Houtkooper, R.H., MacKenzie, E.D., Brooks, D.G., Wanders, R.J., Petit, P.X., Vaz, F.M., and Gottlieb, E. (2008). Cardiolipin provides an essential activating platform for caspase-8 on mitochondria. J. Cell Biol. *183*, 681–696.

Hsu, Y.H., Dumlao, D.S., Cao, J., and Dennis, E.A. (2013). Assessing phospholipase A2 activity toward cardiolipin by mass spectrometry. PLoS One *8*, e59267.

Iyer, S.S., He, Q., Janczy, J.R., Elliott, E.I., Zhong, Z., Olivier, A.K., Sadler, J.J., Knepper-Adrian, V., Han, R., Qiao, L., et al. (2013). Mitochondrial cardiolipin is required for Nlrp3 inflammasome activation. Immunity *39*, 311–323.

Jussupow, A., Di Luca, A., and Kaila, V.R.I. (2019). How cardiolipin modulates the dynamics of respiratory complex I. Sci. Adv. *5*, v1850.

Kagan, V.E., Tyurin, V.A., Jiang, J., Tyurina, Y.Y., Ritov, V.B., Amoscato, A.A., Osipov, A.N., Belikova, N.A., Kapralov, A.A., Kini, V., et al. (2005). Cytochrome c acts as a cardiolipin oxygenase required for release of proapoptotic factors. Nat. Chem. Biol. *1*, 223–232.

Klein Geltink, R.I., O'Sullivan, D., Corrado, M., Bremser, A., Buck, M.D., Buescher, J.M., Firat, E., Zhu, X., Niedermann, G., Caputa, G., et al. (2017). Mitochondrial Priming by CD28. Cell *171*, 385–397.e11, e311.

Konjar, Š., Frising, U.C., Ferreira, C., Hinterleitner, R., Mayassi, T., Zhang, Q., Blankenhaus, B., Haberman, N., Loo, Y., Guedes, J., et al. (2018). Mitochondria maintain controlled activation state of epithelial-resident T lymphocytes. Sci. Immunol. *3*, 3.

Ma, E.H., Verway, M.J., Johnson, R.M., Roy, D.G., Steadman, M., Hayes, S., Williams, K.S., Sheldon, R.D., Samborska, B., Kosinski, P.A., et al. (2019). Metabolic Profiling Using Stable Isotope Tracing Reveals Distinct Patterns of Glucose Utilization by Physiologically Activated CD8$^+$ T Cells. Immunity *51*, 856–870.e5, e855.

Mangat, J., Lunnon-Wood, T., Rees, P., Elliott, M., and Burch, M. (2007). Successful cardiac transplantation in Barth syndrome–single-centre experience of four patients. Pediatr. Transplant. *11*, 327–331.

Mannella, C.A., Pfeiffer, D.R., Bradshaw, P.C., Moraru, I.I., Slepchenko, B., Loew, L.M., Hsieh, C.E., Buttle, K., and Marko, M. (2001). Topology of the mitochondrial inner membrane: dynamics and bioenergetic implications. IUBMB Life *52*, 93–100.

Matyash, V., Liebisch, G., Kurzchalia, T.V., Shevchenko, A., and Schwudke, D. (2008). Lipid extraction by methyl-tert-butyl ether for high-throughput lipidomics. J Lipid Res *49*, 1137–1146.

Mehdipour, A.R., and Hummer, G. (2016). Cardiolipin puts the seal on ATP synthase. Proc. Natl. Acad. Sci. USA *113*, 8568–8570.

Minkler, P.E., and Hoppel, C.L. (2010). Separation and characterization of cardiolipin molecular species by reverse-phase ion pair high-performance liquid chromatography-mass spectrometry. J. Lipid Res. *51*, 856–865.

Mürke, E., Stoll, S., Lendeckel, U., Reinhold, D., and Schild, L. (2016). The mitochondrial phospholipid cardiolipin is involved in the regulation of T-cell proliferation. Biochim. Biophys. Acta *1861* (8 Pt A), 748–754.

Nath, A.K., Ryu, J.H., Jin, Y.N., Roberts, L.D., Dejam, A., Gerszten, R.E., and Peterson, R.T. (2015). PTPMT1 Inhibition Lowers Glucose through Succinate Dehydrogenase Phosphorylation. Cell Rep. *10*, 694–701.

Nicholls, D.G. (2009). Spare respiratory capacity, oxidative stress and excitotoxicity. Biochem. Soc. Trans. *37*, 1385–1388.

O'Sullivan, D., van der Windt, G.J., Huang, S.C., Curtis, J.D., Chang, C.H., Buck, M.D., Qiu, J., Smith, A.M., Lam, W.Y., DiPlato, L.M., et al. (2014). Memory CD8(+) T cells use cell-intrinsic lipolysis to support the metabolic programming necessary for development. Immunity *41*, 75–88.

Paradies, G., Paradies, V., Ruggiero, F.M., and Petrosillo, G. (2014). Cardiolipin and mitochondrial function in health and disease. Antioxid. Redox Signal. *20*, 1925–1953.

Paradies, G., Paradies, V., Ruggiero, F.M., and Petrosillo, G. (2019). Role of Cardiolipin in Mitochondrial Function and Dynamics in Health and Disease: Molecular and Pharmacological Aspects. Cells *8*, 8.

Pearce, E.L., Walsh, M.C., Cejas, P.J., Harms, G.M., Shen, H., Wang, L.S., Jones, R.G., and Choi, Y. (2009). Enhancing CD8 T-cell memory by modulating fatty acid metabolism. Nature *460*, 103–107.

Pernas, L., and Scorrano, L. (2016). Mito-Morphosis: Mitochondrial Fusion, Fission, and Cristae Remodeling as Key Mediators of Cellular Function. Annu. Rev. Physiol. *78*, 505–531.

Pickles, S., Vigié, P., and Youle, R.J. (2018). Mitophagy and Quality Control Mechanisms in Mitochondrial Maintenance. Curr. Biol. *28*, R170–R185.

Puleston, D.J., Zhang, H., Powell, T.J., Lipina, E., Sims, S., Panse, I., Watson, A.S., Cerundolo, V., Townsend, A.R., Klenerman, P., and Simon, A.K. (2014). Autophagy is a critical regulator of memory CD8(+) T cell formation. eLife *3*, 3.

Restifo, N.P., Dudley, M.E., and Rosenberg, S.A. (2012). Adoptive immunotherapy for cancer: harnessing the T cell response. Nat. Rev. Immunol. *12*, 269–281.

Ronghe, M.D., Foot, A.B., Martin, R., Ashworth, M., and Steward, C.G. (2001). Non-Epstein-Barr virus-associated T-cell lymphoma following cardiac transplantation for Barth syndrome. Acta Paediatr. *90*, 584–586.

Schlame, M. (2013). Cardiolipin remodeling and the function of tafazzin. Biochim. Biophys. Acta *1831*, 582–588.

Schlame, M., Kelley, R.I., Feigenbaum, A., Towbin, J.A., Heerdt, P.M., Schieble, T., Wanders, R.J., DiMauro, S., and Blanck, T.J. (2003). Phospholipid abnormalities in children with Barth syndrome. J. Am. Coll. Cardiol. *42*, 1994–1999.

Schwall, C.T., Greenwood, V.L., and Alder, N.N. (2012). The stability and activity of respiratory Complex II is cardiolipin-dependent. Biochim. Biophys. Acta *1817*, 1588–1596.

Sena, L.A., Li, S., Jairaman, A., Prakriya, M., Ezponda, T., Hildeman, D.A., Wang, C.R., Schumacker, P.T., Licht, J.D., Perlman, H., et al. (2013). Mitochondria are required for antigen-specific T cell activation through reactive oxygen species signaling. Immunity *38*, 225–236.

Serricchio, M., Vissa, A., Kim, P.K., Yip, C.M., and McQuibban, G.A. (2018). Cardiolipin synthesizing enzymes form a complex that interacts with cardiolipin-dependent membrane organizing proteins. Biochim. Biophys. Acta Mol. Cell Biol. Lipids *1863*, 447–457.

Steward, C.G., Groves, S.J., Taylor, C.T., Maisenbacher, M.K., Versluys, B., Newbury-Ecob, R.A., Ozsahin, H., Damin, M.K., Bowen, V.M., McCurdy, K.R., et al. (2019). Neutropenia in Barth syndrome: characteristics, risks, and management. Curr. Opin. Hematol. *26*, 6–15.

Sustarsic, E.G., Ma, T., Lynes, M.D., Larsen, M., Karavaeva, I., Havelund, J.F., Nielsen, C.H., Jedrychowski, M.P., Moreno-Torres, M., Lundh, M., et al. (2018). Cardiolipin Synthesis in Brown and Beige Fat Mitochondria Is Essential for Systemic Energy Homeostasis. Cell Metab. *28*, 159–174.e11, e111.

Tschumi, B.O., Dumauthioz, N., Marti, B., Zhang, L., Lanitis, E., Irving, M., Schneider, P., Mach, J.P., Coukos, G., Romero, P., and Donda, A. (2018). CAR T cells are prone to Fas- and DR5-mediated cell death. J. Immunother. Cancer *6*, 71.

van der Windt, G.J., Everts, B., Chang, C.H., Curtis, J.D., Freitas, T.C., Amiel, E., Pearce, E.J., and Pearce, E.L. (2012). Mitochondrial respiratory capacity is a critical regulator of CD8+ T cell memory development. Immunity *36*, 68–78.

Wolf, D.M., Segawa, M., Kondadi, A.K., Anand, R., Bailey, S.T., Reichert, A.S., van der Bliek, A.M., Shackelford, D.B., Liesa, M., and Shirihai, O.S. (2019). Individual cristae within the same mitochondrion display different membrane potentials and are functionally independent. EMBO J. *38*, e101056.

Xu, X., Araki, K., Li, S., Han, J.H., Ye, L., Tan, W.G., Konieczny, B.T., Bruinsma, M.W., Martinez, J., Pearce, E.L., et al. (2014). Autophagy is essential for effector CD8(+) T cell survival and memory formation. Nat. Immunol. *15*, 1152–1161.

Zhang, J., Guan, Z., Murphy, A.N., Wiley, S.E., Perkins, G.A., Worby, C.A., Engel, J.L., Heacock, P., Nguyen, O.K., Wang, J.H., et al. (2011). Mitochondrial phosphatase PTPMT1 is essential for cardiolipin biosynthesis. Cell Metab. *13*, 690–700.

STAR★METHODS

KEY RESOURCE TABLE

REAGENT or RESOURCE	SOURCE	IDENTIFIER
Antibodies		
anti-mouse CD3, inVivoMAb	Bio Cell	Cat#BE0002; RRID: AB_1107630
anti-mouse CD28, inVivoMab	Bio Cell	Cat#BE0015; RRID: AB_1107628
BV421 anti-mouse CD8a	Biolegend	Cat#100738; RRID: AB_11204079
T-select I-Ab OVA Tetramer-PE	MBL	Cat#TS-M710-1
FITC anti-mouse CD45.2	Biolegend	Cat#109806; RRID: AB_313443
PE anti-mouse CD62L	Biolegend	Cat#104408; RRID: AB_313095
APC-Cy7 anti-mouse CD44	Biolegend	Cat#103028; RRID: AB_830785
PerCP/Cyanine5.5 anti-mouse/human KLRG1	Biolegend	Cat#138418; RRID: AB_2563015
AF647 anti-mouse CD127 (IL-7Rα)	Biolegend	Cat#135020; RRID: AB_1937209
AF488 anti-mouse IFNg	Biolegend	Cat#505813; RRID: AB_493312
APC anti-mouse CD5	Biolegend	Cat#100626; RRID: AB_2563929
AF647 anti-mouse CD25	Biolegend	Cat#102020; RRID: AB_493458
PE anti-mouse CD69	Biolegend	Cat#104508; RRID: AB_313111
PE-Cy7 anti-Ki67	Biolegend	Cat#652426; RRID: AB_2632694
AF647 anti-mouse TNF-alpha	Biolegend	Cat#506314; RRID: AB_493330
PE anti-mouse IL-2	Biolegend	Cat#503808; RRID: AB_315302
APC-Cy7 anti-human CD14	Biolegend	Cat#301819; RRID: AB_493694
APC-Cy7 anti-human CD16	Biolegend	Cat#302017; RRID: AB_314217
APC-Cy7 anti-human CD19	Biolegend	Cat#302217; RRID: AB_314247
APC-Cy7 anti-human CD8	Biolegend	Cat#300926; RRID: AB_10613636
APC-Cy7 anti-human CD25	Biolegend	Cat#302613; RRID: AB_314283
BV711 anti-human CD45RO	Biolegend	Cat#304235; RRID: AB_11218600
FITC anti-human IFNg	Biolegend	Cat#502507; RRID: AB_315232
BV421 anti-human CD4	Biolegend	Cat#357423; RRID: AB_2721518
PE anti-human hCD45RO	Biolegend	Cat#304206; RRID: AB_314422
APC anti-human CD45RA	Biolegend	Cat#304112; RRID: AB_314416
AF488 anti-human CD62L	Biolegend	Cat#304816; RRID: AB_528857
BV785 anti-human CD197	Biolegend	Cat#353229; RRID: AB_2561371
PE-Cy7 anti-humna CD95	Biolegend	Cat#305621; RRID: AB_2100370
BV711 anti-human CD28	Biolegend	Cat#302947; RRID: AB_2616856
PE-Cy7 anti-human CD4	Biolegend	Cat#357409; RRID: AB_2565661
BV711 anti-human CD25	Biolegend	Cat#302635; RRID: AB_11219793
AF647 anti-human IFNg	Biolegend	Cat#502516; RRID: AB_493031
APC-Cy7 anti-human CD56	Biolegend	Cat#318331; RRID: AB_10898118
BV605 anti-mouse TCRb	Biolegend	Cat#109241; RRID: AB_2629563
APC anti-mouse TCR gammadelta	Biolegend	Cat#118115; RRID: AB_1731824
PE-Cy7 anti-mouse CD8b	Biolegend	Cat#140416; RRID: AB_2564385
OPA1	BD Biosciences	Cat#612606; RRID: AB_399888
ACONITASE	Abcam	Cat#ab126595; RRID: AB_11130595
SDHA	Cell Signaling	Cat#11998S; RRID: AB_2750900
IDH	Cell Signaling	Cat#8137S; RRID: AB_10950504
SCS	Cell Signaling	Cat#5557S; RRID: AB_10691593
CPT1a	Proteintech	Cat#15184-1-AP; RRID: AB_2084676
TUBULIN	Cell Signaling	Cat#2144S; RRID: AB_2210548

(Continued on next page)

Continued

REAGENT or RESOURCE	SOURCE	IDENTIFIER
CALNEXIN	Santa Cruz	Cat#sc-23954; RRID: AB_626783
GAPDH	Cell Signaling	Cat#5174P; RRID: AB_10622025
TAFAZZIN	Santa Cruz	Cat#sc-365810; RRID: AB_10842049
CRLS1	Abcam	Cat#ab156882
TOM20	Cell Signaling	Cat#42406; RRID: AB_2687663
MnSOD	Enzo LifeScience	Cat#ADI-SOD-110-F; RRID: AB_2750987
OXPHOS cocktail	Abcam	Cat#ab110413; RRID: AB_2629281
ACTIN	Cell Signaling	Cat#4970; RRID: AB_2223172
PTPMT1	Sigma	Cat#HPA043932; RRID: AB_2678738
Bacterial and Virus Strains		
LmOVA ΔActa	N/A	N/A
LmOVA WT	N/A	N/A
Biological Samples		
Healthy control blood	UniKlinik Freiburg	N/A
Chemicals, Peptides, and Recombinant Proteins		
ImmunoCult™ Human CD3/CD28/CD2 T Cell Activator	StemCell Technologies, Inc.	Cat#10990
Fixation/Permeabilization Solution Kit	BD	Cat#554714
Mitotracker green FM	Thermofisher Scientific	Cat#M7514
TMRM	Thermofisher Scientific	Cat#T668
D-GLUCOSE-13C6, 99 ATOM % 13C, ^{3}99%	Sigma	Cat#389374
LINOLEIC ACID-13C18, 99 ATOM % 13C, 97%+	Sigma	Cat#605735
Alexidine dihydrochloride	Sigma	Cat#A8986
PMA	Sigma	Cat#P1585
Ionomycin calcium salt	Sigma	Cat#I3909
Anti-Rat IgG (Fc specific)-Biotin antibody	Sigma	Cat#SAB3700543
Indo-1 AM	Thermofisher Scientific	Cat#I1223
Thapsigarargin	Tocris	Cat#1138
Fx cycle	Thermofisher Scientific	Cat#R37166
LIVE/DEAD™ Fixable Aqua Dead Cell Stain Kit	Thermofisher Scientifi	Cat#L34957
LIVE/DEAD™ Fixable IR Dead Cell Stain Kit	Thermofisher Scientific	Cat#L34975
Cell Trace Violet Proliferation Kit	Thermofisher Scientific	Cat#C34557
Recombinant human IL-2	Peprotech	Cat#200-02
Recombinant murine IL-15	Peprotech	Cat#210-15
PG(18:1)2	Avanti Lipids	Cat#840475
PG(18:2)2	Avanti Lipids	Cat#840485
Oligomycin	Sigma	Cat#1404-19-9
FCCP	Sigma	Cat#370-86-5
Tamoxifen	Sigma	Cat#T5648
Rotenone	Sigma	Cat#83-79-4
Antimycin A	Sigma	Cat#1397-94-0
Alt-R® S.p. Cas9 Nuclease V3	IDT	Cat#1081059
Brefeldin A solution	BioLegend	Cat#BLD-420601
Brain Heart infusion Broth (BHI)	Sigma	Cat#53286
Cysclosporine H	Sigma	Cat#SML1575
7-AAD Viability Staining Solution	BioLegend	Cat#420404

(Continued on next page)

Continued

REAGENT or RESOURCE	SOURCE	IDENTIFIER
Critical Commercial Assays		
EasySep Mouse CD8+ TCell Isolation Kit	StemCell Technologies, Inc.	Cat#19853
EasySep Human CD45RO+ CD8+ T Cell Isolation Kit	StemCell Technologies, Inc.	Cat#19159
EasySep Human CD45RA+ CD8+ T Cell Isolation Kit	StemCell Technologies, Inc.	Cat#19258
High Capacity cDNA Reverse Transcription Kit	Thermofisher Scientific	Cat#4368814
iTaq Universa Probes Supermix	Bio-Rad	Cat#1725131
Pierce BCA protein assay kit	Thermofisher Scientific	Cat#23225
Experimental Models: Organisms/Strains		
C57BL/6J mice	Jackson laboratories	RRID: IMSR_JAX:000664
PTPMT1 floxed mice	Jackson laboratories	RRID: IMSR_JAX:020775
PhAM mice	Jackson laboratories	RRID: IMSR_JAX:018397
OT-I mice	Jackson laboratories	RRID: IMSR_JAX:003831
CD45.1 congenic mice	Jackson laboratories	RRID: IMSR_JAX:002014
TAZ KO	Dr. Douglas Strathdee	N/A
Oligonucleotides		
PTPMT1 sgRNA1	IDT	Mm.Cas9.PTPMT1.1.AA
PTPMT1 sgRNA2	IDT	Mm.Cas9.PTPMT1.1.AB
PTPMT1 sgRNA3	IDT	Mm.Cas9.PTPMT1.1.AC
TAZ sgRNA1	IDT	Mm.Cas9.TAZ.1.AA
TAZ sgRNA2	IDT	Mm.Cas9.TAZ.1.AB
TAZ sgRNA3	IDT	Mm.Cas9.TAZ.1.AC
TaqMan Gene expression Assay, Assay ID: Mm00504978_m1 TAZ FAM-MGB	Applied Biosystem	Cat#4448892
TaqMan Gene expression Assay, Assay ID: Mm04225274_s1 Gene Symbol: ND1 FAM-MGB	Applied Biosystem	Cat#4331182
TaqMan Gene Expression Assay, Assay ID: Mm03024075_m1 Gene: Hprt, FAM-MGB	Applied Biosystem	Cat#4351368
Recombinant DNA		
Plasmid: pMAX-GFP (control vector in nucleofector kit)	LONZA	N/A
Software and Algorithms		
Wave software version 2.4	Agilent	http://www.agilent.com/cs/ContentServer?c=Page&pagename=Sapphire/Page/HomePage
FlowJO	FlowJO	https://www.flowjo.com
Graphpad Prism 7 (seahorse and statistical analysis)	Graphpad software	http://www.graphpad.com
ImageJ	NIH	N/A

RESOURCE AVAILABILITY

Lead Contact
Further information and requests for resources and reagents should be directed to and will be fulfilled by the Lead Contact, Erika L. Pearce (pearce@ie-freiburg.mpg.de)

Materials Availability
This study did not generate new unique reagents

Data and Code Availability
This study did not generate datasets

EXPERIMENTAL MODEL AND SUBJECT DETAILS

Cell Culture and Drug Treatment
Mouse Cells
CD8$^+$ T cells were isolated from spleens of 8-10 week-old mice using the naive or bulk CD8$^+$ T cell kit (Stem Cell technologies, Cat# 19858, 19853) according to the manufacturers protocol. Both male and female mice were used and within experiments mice were age and sex matched. Sample size is indicated in the figure legends. Isolated T cells were activated using plate bound αCD3 (5 μg/mL) (anti-mouse CD3, inVIVOMAb Cat# BE0002), in 1640 media supplemented with 10% fetal calf serum, 4mM L-glutamine, 1% penicillin/streptomycin, 100 U/mL hrIL-2 (Peprotech), 55 μM beta-mercaptoethanol, and ± 0.5 μg/mL soluble αCD28 (anti-mouse CD28, inVivoMab Cat# BE0015) under 5% CO$_2$, atmospheric oxygen, at 37°C in a humidified incubator. T$_E$ and T$_M$ cell differentiation was performed as previously described (Buck et al., 2016). Briefly, media changes were performed from day 2 post activation and then daily up to day 6. For T$_E$ cell differentiation cells were incubated in 100 U/mL hrIL-2 (Peprotech), for T$_M$ cells in 100U/mL mIL-15 (Peprotech). Where indicated cells were treated with vehicle control (DMSO or EtOH) or 1 μM Alexidine dihydrochloride (AD, Sigma, A8986), 50 μM PG(18:2)2 (Cat# 840485), PG(18:1 Δ9-cis)2 (Cat# 840475), 5nM 4-OHT. For in vitro survival assays, cells were activated for 3 days as described, then cultured in either IL-2 at 5x10^4 cells/mL, or in IL-15 at 1x10^5 cells/mL in 96 well round bottom plates. Survival was analyzed by 7-AAD exclusion using flow cytometry.

Human Cells
Fresh buffy coats from healthy donors were kindly provided by the Institute for Transfusion Medicine and Gene Therapy, Medical Center, University of Freiburg under approval by the ethical committee of the University of Freiburg. PBMCs from healthy donors and Barth Syndrome patients were collected at University of Bristol in accordance with the Helsinki Declaration with approval from the UK NHS Research Ethics committee (permit number 09/H0202/52). Age and sex of healthy donors provided by the Institute for Transfusion Medicine and Gene Therapy, Medical Center, University of Freiburg were blinded to the authors. Barth syndrome patients were males (Barth syndrome group average age 13 years, min 6 years, max 28 years; healthy donor group average age 28 years, min 22 years, max 39 years). Informed consent was provided by all patients, or by their parents, in the case of children. Human CD45RA$^+$ and CD45RO$^+$ CD8$^+$ T cells were isolated using CD8$^+$ T cell kits (Stem Cell technologies, Cat# 19258, 19159). Researchers were blinded to the identity of the donors, and age or sex matching was not performed. Sample size is indicated in the figure legends.

Mice and Immunizations
C57BL/6J (RRID: IMSR_JAX:000664), PhAM (RRID: IMSR_JAX:018397), major histocompatibility complex (MHC) class I-restricted OVA specific TCR OT-I transgenic mice (RRID: IMSR_JAX:003831), and CD45.1 congenic (RRID: IMSR_JAX:002014) mouse strains were purchased from The Jackson Laboratory. PTPMT1 floxed (RRID: IMSR_JAX:020775) mice were a kind gift form Jack E. Dixon (University of California, San Diego, CA). TAZ KO mice were generated and maintained at the University of Glasgow by D. Strathdee under license approved by University of Glasgow Ethical Review Process and the UK Animal Procedures Committee London. PTPMT1 floxed mice were crossed to CD4-Cre or tamoxifen inducible ERT2-Cre mice. Experimental studies including mice of the PTPMT1 strain were approved by the Regierungspräsidium Freiburg. All mice were maintained in C56Bl6/J background and were the results in in-house matings. In all experiments including WT and KO mice, WT littermates from same breedings were used as controls. All mice, apart from TAZ KO, were maintained at the Max Planck Institute of Immunobiology and Epigenetics and cared for according to the Institutional Animal Use and Care Guidelines. Briefly, mice were maintained in IVC Tecniplast green line cages with max five mice per cage, light cycle was 14/10 h, temperature 20-24°C, humidity 45%–64%. Ssniff MZ-Ereich chow (Cat# V1185-300) was provided ad libitum. Health monitoring program followed FELASA recommendations (Laboratory Animals 2014, Vol. 48(178-192). Briefly, germ free NMRI mice are used as bedding sentinels receiving dirty bedding from up to 100 other cages weekly for three months before being tested for all pathogens and opportunists recommended in the guidelines. Within experiments, age and sex matched mice were injected intravenously (i.v.) as indicated with a sublethal dose of 1x10^6 colony forming units (CFU) of recombinant L. monocytogenes expressing OVA deleted for actA (LmOVA ΔActa) for primary immunizations and challenged with 5x10^7 CFU for secondary immunizations. Where indicated, 3x10^4 CFU of L. monocytogenes expressing OVA WT were used for primary infection and 1x10^6 for secondary immunization.

   All mice were used for experiments between 8-10 weeks of age apart from TAZ KO mice that were 20 weeks old (time in which pathology develops) and animals used for T$_{EM}$ and T$_{CM}$ cell sorting that were 20-month old (in order to obtain a sufficient proportion of both T$_{EM}$ and T$_{CM}$ cells from the same animal, 20% and 40% respectively (in 2-month old mice T$_{EM}$ cells constituted only 5% of total CD8$^+$ T cells). For in vivo experiments male mice were used, for in vitro studies both sexes were used interchangeably (no influence or association of sex on the results was observed).

METHODS DETAILS

Bacterial Burden
Liver biopsies were weighed and homogenized in 1ml of PBS. 10 μL per serial dilution of the original homogenate was plated on a Brain Heart infusion Broth (BHI, Sigma Cat# 53286) agar and incubated over night at 37°C. One day later the number of colonies were counted and normalized to the weight of the liver biopsy.

Adoptive Transfers

For *in vivo* T_M cell experiments, £$1x10^4$ OT-I+ CD8$^+$ T cells/mouse from donor splenocytes were transferred intravenously (i.v.) into congenic recipient mice. Blood or spleens were collected at indicated time points and analyzed by flow cytometry. For *in vivo* survival experiments, 1-2x10^6 treated IL-2 T_E cells (6 days post activation) cells/mouse were injected i.v. into naive congenic CD45.1 mice. Cells were recovered at indicated time points from the spleen or lymph nodes and analyzed by flow cytometry.

Flow Cytometry

Fluorochrome-conjugated monoclonal antibodies were purchased from eBioscience, BD PharMingen, or Biolegend. Staining was performed in 1% FBS/PBS for 30 min on ice, dead cells were excluded with the LIVE/DEAD Fixable Aqua Dead Cell Stain Kit (Thermo scientific). OVA-specific CD8$^+$ T cells from spleen, lymph node, or blood were quantified after red blood cell lysis by direct staining with H2-K^{b}OVA$_{257-264}$ (K^{b}OVA) MHC-peptide tetramers. For intracellular cytokine staining cells were reactivated with αCD3/αCD28 overnight or 50 ng/mL phorbol 12-myristate 13-acetate (PMA) + 500 ng/mL ionomycin (all Sigma) for 4 h and cultured in the presence of Brefeldin A for 4 h prior to fixation using Cytofix Cytoperm (BDBioscience). MitoTracker and TMRM staining were performed according to the manufacturer's instructions (Life Technologies) using respectively 10nM and 2nM of Mitotracker Green and TMRM in presence of 0.5 μM of Cysclosporine H. Cells were collected on Fortessa flow cytometers (BD Biosceince) and analyzed using FlowJo software (FlowJo).

Confocal and Electron Microscopy Imaging

Spinning disk confocal and EM imaging was performed as described previously (Buck et al., 2016). Cells were activated as indicated and transferred to glass bottom dishes (MatTek) coated with fibronectin(Sigma) in complete medium containing IL-2 or IL-15 using a Zeiss spinning disk confocal with an Evolve (EMCCD) camera. Cells were kept in a humidified incubation chamber at 37°C with 5% CO_2 during image collection. Confocal imaging was analyzed using Imaris imaging software. For Electron Microscope imaging 2 × 10^6 T cells were fixed in 2.5% glutaraldehyde in 100 mM sodium cocodylate, washed in cocodylate buffer. After dehydration samples were embedded in Eponate 12 resin (Ted Pella) and sections were cut. Images were acquired using a FEI Tecnai 12 Transmission electron microscope equipped with a TIETZ digital camera. Cristae width was measured using ImageJ software and averaged over 50 independent images, acquisition of EM micrographs and measurements of max cristae width displayed were performed using ImageJ software (NIH). Brightness and contrast were adjusted in ImageJ software (NIH)

Metabolic Phenotyping

Oxygen consumption rates (OCR) and extracellular acidification rates (ECAR) were measured in XF media (non-buffered RPMI 1640 containing 25 mM glucose, 2mM L-glutamine, and 1 mM sodium pyruvate) under basal conditions and in response to 1 μM oligomycin, 1.5 μM fluoro-carbonyl cyanide phenylhydrazone (FCCP) and 100 nM rotenone + 1 μM antimycin A, or 50 ng/mL phorbol 12-myristate 13-acetate (PMA) + 500 ng/mL ionomycin (all Sigma) using a 96 well XF or XFe Extracellular Flux Analyzer (EFA) (Seahorse Bioscience). 2 x10^5 T cells per well (^{3}3 wells per sample) were spun onto poly-D-lysine coated seahorse 96 well plates and preincubated at 37°C for a minimum of 45 min in the absence of CO_2. For activation of T cells, αCD3 ± CD28 coated beads were used at 1:1 ratio of beads:T cell Thermofisher, Cat# 11452D). For metabolic tracing naive (T_N) cells (Figure 4) were isolated and activated as described above in glucose-free media supplemented with 11 mM D-[U^{13}C] glucose or 11mM unlabeled D-glucose for 24 h. Cells were washed with ice cold 0.9% w/v NaCl buffer and metabolites were extracted three times with cold methanol (80%) and analyzed by GCMS. For glucose and palmitate tracing into CL, T cells were cultured in IL-2 or IL-15 condition in presence of 11 mM D-[U^{13}C] glucose or 20 μM [U^{13}C]-Palmitate for 72 h. Medium was changed daily. Cell pellets for lipid extraction were collected at indicated time points.

Lipid Extraction and Quantification

Lipids were extracted using a biphasic Methyl *tert*-butyl ether (MTBE) extraction protocol (adapted from Matyash et al., 2008). In brief, cells were resuspended in 100uL cold PBS in glass vials. Cold methanol (750uL), MTBE (2mL), and water (625uL) were added sequentially with vortexing. Samples were centrifuged to separate phases, and the upper organic phase was dried using a Genevac EZ2 speed vac. Samples were resuspended in 2:1:1 isopropanol:acetonitrile:water prior to analysis. LC-MS was carried out using an Agilent Zorbax Eclipse Plus C18 column using an Agilent 1290 Infinity II UHPLC in line with an Agilent 6495 Triple Quad QQQ-MS. Lipids were identified by fragmentation and retention time, and were quantified using Agilent Mass Hunter software.

Glucose and Linoleic Acid Tracing into Cardiolipin

Label tracing by LC-MS was carried out using an Agilent 1290 Infinity II UHPLC inline with a Bruker Impact II QTOF-MS operating in negative ion mode. Scan range was from 50 to 1600 Da. Mass calibration was performed at the beginning of each run. LC separation was on a Zorbax Eclipse plus C18 column (100 × 2 mm, 1.8 μm particles) using a solvent gradient of 70% buffer A (10 mM ammonium formiate in 60:40 acetonitrile:water) to 97% buffer B (10 mM ammonium formiate in 90:10 2-propanol:acetonitrile). Flow rate was from 400 μL/min, autosampler temperature was 5°C and injection volume was 2 μL. Data processing including correction for natural isotope abundance was carried out by an in-house R script.

Glucose Tracing into Central Carbon Metabolites

Dried metabolite extracts were resuspended in pyridine and derivatized with methoxyamine (sc-263468 Santa Cruz Bio) for 60 min at 37°C and subsequently with N-(tert-butyldimethylsilyl)-N-methyl-trifluoroacetamid, with 1% tert-utyldimethylchlorosilane (375934 Sigma-Aldrich) for 30 min at 80°C. Isotopomer distributions were measured using a DB5-MS GC column in a 7890 GC system (Agilent Technologies) combined with a 5977 MS system (Agilent Technologies). Data processing, including correction for natural isotope abundance was performed by an in-house R script.

RT-PCR

RNA isolations were done by using the RNeasy kit (QIAGEN) and single-strand cDNA was synthesized using the High Capacity cDNA Reverse Transcription Kit (Applied Biosystems). All RT-PCR were performed using iTaq Universa Probes Supermix (Biorad) and Taq-man primers (Thermo Fisher Sceintific) using an Applied Biosystems 7000 sequence detection system. The expression levels of mRNA were normalized to the expression of a housekeeping gene (HPRT ot ActB).

mtDNA/nDNA Quantification

Genomic DNA was extracted with QIAGEN QIAamp DNA Micro Kit. DNA was quantified, diluted to 10ng/μl and 50 μg of DNA was used for qPCR analysis of mtDNA (*ND1*) and nuclear DNA transcripts (*Hprt*).

Calcium Flux

CD8$^+$ T cells were isolated using CD8$^+$ T cell kit (Stem Cell technologies, Cat# 19853). 3*10^6 cells were loaded 30min at 37°C in humidified incubator with 2uM Indo-AM dissolved in complete medium + 0,5 μM CsH. Then, cells were washed and resuspended in 300 μL of complete medium supplemented with 0,5 μM CsH and 5 μg/mL anti-mouse CD3 (inVivoMAb Cat# BE0002) 30min at 4°C in the dark. At cytofluorimeter indoviolet and indoblue were acquired in linear scale. Tube was placed in 37°C temperature-controlled tube holder immediately before acquisition and signal was acquired as follows: 30 s basal, 6min after addition of Anti-Rat IgG (Fc-specific)biotin crosslinking antibody (Sigma, SAB3700543, diluted 1:50 directly in the acquisition tube), 2 min after adding tapsigargin (final concentration 100nM) to measure endoplasmic reticulum calcium stores depletion, 1min after adding Ionomycin (final concentration 500 ng/mL) to evaluate maximal calcium flux.

Cell Cycle Analysis

At indicated time points after activation CD8$^+$ T cells were stained with NearIR Live dead staining (Thermofisher) 10min RT in the dark, fixed in fixative buffer from eBioscience Foxp3 / Transcription Factor Staining Buffer Set (00-5523-00) for 60min at RT. After a wash in perm buffer, cells were stained with PE-Cy7 Anti-Ki67 antibody in perm buffer 45min 4°C in the dark. After additional wash cells were resuspended in FxCycle (Thermofisher R37166) diluted 1:4000 in PBS immediately before flow cytometry acquisition.

Western Blotting

For western blot analysis, cells were washed with ice cold PBS and lysed in 1 x Cell Signaling lysis buffer (20 mM Tris-HCL [pH 7.5], 150 mM NaCl, 1 mM Na$_2$EDTA, 1mM EGTA, 1% Triton X-100, 2.5 mM sodium pyrophosphate, 1 mM β-glycerophosphate, 1mM Na$_3$VO$_4$, 1 μg/mL leupeptin), supplemented with 1mM PMSF for 30min followed by centrifugation at 20.000 x g for 10 min at 4°C. Cleared protein lysate were quantified using Pierce BCA protein assay kit (Cat#23225) according to manufacturer's instruction. Cleared protein extracts were denatured with LDS loading buffer for 10 min at 70°C and loaded onto precast 4% to 12% bis-tris protein gels. Proteins were transferred onto nitrocellulose membranes using the iBLOT2 system following the manufacturers protocols. Membranes were blocked with 5% w/v milk and 0.1% Tween-20 in TBS and incubated with the appropriate antibodies in 5% w/v BSA in TBS with 0.1% Tween-20 overnight at 4°C. All primary antibody incubations were followed by incubation with secondary HRP-conjugated antibody (Pierce) in 5% milk and 0.1% Tween-20 in TBS and visualized using SuperSignal West Pico or Femto Chemiluminescent Substrate (Pierce) on Biomax MR Film (Kodak). Optical density of the signals on the film was quantified using grayscale measurements in ImageJ software (NIH) and converted to fold change, normalized to the loading control.

Generation of CRISPR KO T Cells

CD8$^+$ T cells were electroporated using Amaxa electroporation system with 60 nmol of sgRNA-CAS9 (Alt-R® S.p. Cas9 Nuclease V3) complexes (sgRNAs: Mm.Cas9.TAZ.1AA, Mm.Cas9.TAZ.1AB, Mm.Cas9.TAZ.1C targeting TAZ, Mm.Cas9.PTPMT1.1.AA, Mm.Cas9.PTPMT1.1.AB, Mm.Cas9.PTPMT1.1.AC targeting PTPMT1) following manufacturer's guidelines. Naive CD8$^+$ T cells were cultured for 24 h in IL-7 before being activated with αCD3/αCD28 + IL-2.

QUANTIFICATION AND STATISTICAL ANALYSIS

Flow cytometry data were analyzed using FlowJo 10 (BD Biosciences). Statistical Analyses were performed using Prism 7 software (GraphPad) and results are represented as Mean ± SEM, unless otherwise indicated. Comparisons for two groups were calculated using unpaired two-tailed Student's t tests. Comparisons of more than two groups were calculated using one-way ANOVA with Tukey multiple comparison tests. We observed normal distribution and no difference in variance between groups in

individual comparisons. Selection of sample size was based on extensive experience with metabolic assays. The sample size for *in vivo* experiments was based on previous experience with infection experiments. The number of independent experiments performed, and the p values for each experiment are reported in the corresponding figure legends. For both *in vitro* and *in vivo* experiments, no initial exclusion criteria were used and no animals or replicates were excluded from the study.